International Journal of Solids and Structures 64–65 (2015) 100–119

Contents lists available at ScienceDirect

International Journal of Solids and Structures

journal homepage: www.elsevier.com/locate/ijsolstr

A model for porous single crystals with cylindrical voids of elliptical cross-section

A. Mbiakop, A. Constantinescu, K. Danas *

Laboratoire de Mécanique des Solides, CNRS UMR7649 & Département de Mécanique, École Polytechnique, 91128 Palaiseau Cedex, France

ARTICLE INFO

Article history:
Received 14 November 2014
Received in revised form 13 March 2015
Available online 31 March 2015

Keywords:
Crystal plasticity
Porous materials
Homogenization

ABSTRACT

This work presents a rate-dependent constitutive model for porous single crystals with arbitrary number of slip systems and orientations. The single crystal comprises cylindrical voids with elliptical cross-section at arbitrary orientations and is subjected to general plane-strain loadings. The proposed model, called modified variational model (MVAR), is based on the nonlinear variational homogenization method, which makes use of a linear comparison porous single crystal material to estimate the response of the nonlinear porous single crystal. The MVAR model is validated by periodic finite element simulations for a large number of parameters including general in-plane crystal anisotropy, general in-plane void shapes and orientations, various creep exponents (i.e., nonlinearity) and general plane strain loading conditions. The MVAR model, which at the present state involves no calibration parameters, is found to be in good agreement with the finite element results for all cases considered in this work. The model is then used in a predictive manner to investigate the complex response of porous single crystals in several cases with strong coupling between the anisotropy of the crystal and the (morphological) anisotropy induced by the shape and orientation of the voids.

1. Introduction

Voids originating in the manufacturing process have an important effect on the lifetime as well as deformability of materials and play an important role on the constitutive response of metallic alloys. Indeed, as recently indicated by experimental observations (Srivastava et al., 2012) at high enough temperatures on tensile specimens, the growth of initially present processing induced voids in a nickel based single crystal superalloy as well as in standard polycrystals played a significant role in limiting creep life. The presence of voids (or cracks) in metals is known to be one of the major causes of ductile failure, as addressed in pioneering works by Mc Clintock (1968), Rice and Tracey (1969) and Gurson (1977). Most of the studies so far have been carried out in the context of two-phase material systems comprising an isotropic rate-(in) dependent matrix phase (metal usually described by von Mises yield criterion or creep potential) and a voided phase (pores of spherical, spheroidal or arbitrary ellipsoidal shapes). The models proposed previously for ductile damage growth use either limit analysis (see for instance Tvergaard and Needleman, 1984; Gologanu and Leblond, 1993; Leblond et al., 1994; Monchiet et al., 2007; Madou and Leblond, 2012a,b) based on Gurson (1977) work, or a variational homogenization theory using the concept of a linear comparison composite (see for instance Ponte Castañeda, 1991a; deBotton and Ponte Castañeda, 1995; Danas and Ponte Castañeda, 2009a).

Far fewer results have been obtained for rate-(in) dependent anisotropic matrix systems, generally based on a phenomenological Hill-type matrix (see Benzerga and Besson, 2001; Benzerga et al., 2004; Monchiet et al., 2008; Keralavarma et al., 2011). The case of porous single crystals have only been studied through discrete dislocations dynamic by Huang et al. (2007, 2012), Hussein et al. (2008), Segurado and Llorca (2010) and molecular dynamics at smaller scales (Traiviratana et al., 2008; Zhao et al., 2009; Tang et al., 2010a,b), or using finite element simulations (Yerra et al., 2010; Ha and Kim, 2010). Such anisotropic matrix systems have known slip directions and contain usually a small volume fraction of impurities. When these material systems are subjected to external loads impurities fail or decohere leading to the creation of pores, which in turn evolve in size, shape and orientation (Srivastava and Needleman, 2012). This complex evolution of microstructure together with the evolution of the rate-dependent matrix anisotropy is critical in the prediction of the eventual

* Corresponding author.
E-mail addresses: mbiakop@lms.polytechnique.fr (A. Mbiakop), andrei.constantinescu@lms.polytechnique.fr (A. Constantinescu), kdanas@lms.polytechnique.fr (K. Danas).

http://dx.doi.org/10.1016/j.ijsolstr.2015.03.017
0020-7683/

fracture of the specimen under monotonic and cyclic loading conditions.

Nevertheless, there have been only a handful of models for porous single crystals which deal with special void geometries, loading conditions and slip system orientations. Such studies involve the study of cylindrical voids with circular cross-section in a rigid-ideally plastic face-centered cubic (FCC) single crystals using slip line theory (Kysar et al., 2005; Gan et al., 2006; Gan and Kysar, 2007), the study two dimensional "out of plane" cylindrical voids with circular cross-section subjected to anti-plane loadings (Idiart and Ponte Castañeda, 2007) and that of spherical voids (Han et al., 2013; Paux et al., 2015). While each one of these studies has its own significant contribution to the understanding of the effective response of porous single crystals none of them is general enough in the sense of arbitrary void shapes and orientations and general loading conditions.

In this regard, the scope of the present work is to develop a two-dimensional model in plane-strain loading conditions that is able to deal with general in-plane crystal anisotropy, arbitrary elliptical void shapes and orientations and general plane strain loading conditions. While this model is not three-dimensional it represents a necessary step towards this direction. It allows for a fully analytical treatment of the problem and thus provides a good insight of the effective response in such highly nonlinear and highly anisotropic systems. A three-dimensional model is then feasible using the same theory that is developed in the present work and.

More specifically, in Section 2, we use the variational linear comparison composite theory of Ponte Castañeda (1991a) to provide a fully analytical model, called the modified variational (MVAR) model (see Danas and Aravas, 2012), in two-dimensions. Subsequently, in Section 4, we present in detail the finite element (FE) periodic unit-cells which will be used to assess the MVAR model as well as to visualize the underlying deformation fields in the context of porous single crystals. In Sections 5 and 6, we present comparison between the MVAR predictions and the FE results for a wide range of crystal anisotropy, arbitrary elliptical void shapes and orientations, porosities, creep exponents and general plane-strain loading conditions. Finally, we conclude with Section 7.

2. Theory

Consider the RVE (representative volume element) Ω to be a two-phase porous single crystal with each phase occupying a sub-domain $\Omega^{(r)}$ $(r=1,2)$. The vacuous phase is identified with phase 2 and the non-vacuous phase (i.e., single crystal matrix) is denoted as phase 1. At this point it is important to note that we make use of the hypothesis of separation of length scales which implies that the size of the voids (microstructure) is much smaller than the size of the single crystal and the variation of the loading conditions at the level of the single crystal. In the following, the brackets $\langle\cdot\rangle$ and $\langle\cdot\rangle^{(r)}$ define volume averages over the RVE (Ω) and the phase r ($\Omega^{(r)}$), respectively.

2.1. Microstructure

The present study focuses on two-dimensional (2D) porous single crystals containing polydisperse cylindrical voids aligned with the x_3-axis. The voids are randomly and uniformly distributed in the transverse plane x_1–x_2. This material is subjected to plane-strain loading in the x_3-direction. In this regard, we first define the relevant microstructural variables, which serve to describe the volume fraction of the vacuous phase as well as the shape, orientation and the distribution of the voids embedded uniformly in the matrix phase. For simplicity, we will also consider that the shape and orientation of the distribution function is identical to the shape and orientation of the voids themselves (see Danas and Ponte Castañeda, 2009a). However, this analysis can be readily extended to distribution of a different shape and orientation than the voids (Ponte Castañeda, 1995; Kailasam and Ponte Castañeda, 1998). Thus, as shown in Fig. 1, the internal variables characterizing the state of the microstructure are:

- The porosity or volume fraction of the voids $f=V_2/V$, where $V=V_1+V_2$ is the total volume, with V_1 and V_2 being the volume occupied by the matrix and the vacuous phase, respectively.
- The aspect ratio $w=a_2/a_1$, with $2a_i$ $(i=1,2)$ denoting the lengths of the principal axes of the representative elliptical void, in the plane $1-2$. The cases $w=1$ and $w\neq 1$ correspond to voids with circular and elliptical cross-sections, respectively.
- The in-plane orientation unit vectors $\mathbf{n}^{(i)}$ $(i=1,2)$, defining an orthonormal basis set, which coincides with the principal axes of the representative elliptical void. As a consequence of the 2D representation of the microstructure the two orientation vectors $\mathbf{n}^{(i)}$ can be easily parameterized in terms of a single Euler angle, ψ,

$$\mathbf{n}^{(1)}=\cos\psi\,\mathbf{e}_1+\sin\psi\,\mathbf{e}_2,\quad \mathbf{n}^{(2)}=-\sin\psi\,\mathbf{e}_1+\cos\psi\,\mathbf{e}_2. \tag{2.1}$$

The above set of the microstructural variables can then be denoted by the set $s_\alpha=\{f,w,\psi\}$.

2.2. Effective behavior: general considerations

The local constitutive behavior of the matrix phase is characterized by an anisotropic, convex stress potential $U_1\equiv U$ while the stress potential of the porous phase $U_2\equiv 0$. As a consequence of the Hill–Mandel lemma (Hill, 1963; Mandel, 1964), the effective stress potential $\widetilde{U}$ for a porous medium is reduced to

$$\widetilde{U}(\overline{\boldsymbol{\sigma}},s_\alpha)=(1-f)\min_{\boldsymbol{\sigma}\in S(\overline{\boldsymbol{\sigma}})}\langle U(\boldsymbol{\sigma})\rangle^{(1)}, \tag{2.2}$$

where

$$S(\overline{\boldsymbol{\sigma}})=\left\{\boldsymbol{\sigma},\operatorname{div}(\boldsymbol{\sigma})=0\text{ in }\Omega,\ \boldsymbol{\sigma}\mathbf{n}=0\text{ on }\partial\Omega^{(2)},\ \langle\boldsymbol{\sigma}\rangle=\overline{\boldsymbol{\sigma}}\right\} \tag{2.3}$$

is the set of statically admissible stresses that are compatible with the average stress $\overline{\boldsymbol{\sigma}}$ and a traction free void surface.

Subsequently, the effective strain-rate tensor can be expresses as

$$\overline{\mathbf{D}}=\frac{\partial\widetilde{U}}{\partial\overline{\boldsymbol{\sigma}}}(\boldsymbol{\sigma}). \tag{2.4}$$

The above described problem is non-trivial since it involves, in general, nonlinear constitutive relations for the constituents as well as random spatial distributions of the voids and thus the goal of the present work is to propose approximate, albeit robust and rigorous, homogenized models. In the next sections, we define the local constitutive response of the single crystal matrix and we provide both analytical and numerical estimates of the effective response of such porous single crystals.

2.3. Constitutive behavior of the constituents

Let us consider a reference single crystal which undergoes viscoplastic deformation on a set of K preferred crystallographic slip systems. At this stage, for simplicity in the homogenization procedure elasticity effects are neglected. Then, these systems are

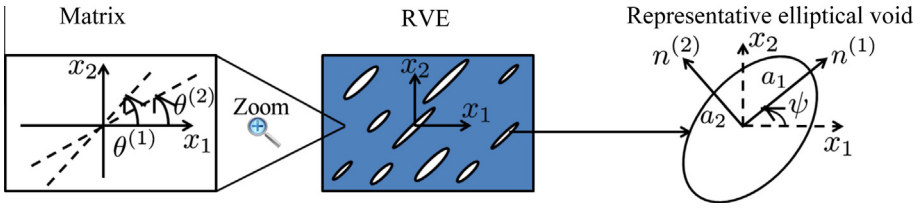

Fig. 1. Representative elliptical cross-section voids embedded in a crystal matrix.

characterized by the second-order Schmid tensors $\boldsymbol{\mu}^{(s)}$ $(\forall s = 1,\dots,K)$ given by

$$\boldsymbol{\mu}^{(s)} = \frac{1}{2}\left(\mathbf{m}^{(s)} \otimes \mathbf{s}^{(s)} + \mathbf{s}^{(s)} \otimes \mathbf{m}^{(s)}\right), \tag{2.5}$$

where $\mathbf{m}^{(s)}$ and $\mathbf{s}^{(s)}$ are the unit vectors normal to the slip plane and along the slip direction in the sth system, respectively. Moreover, it is assumed that the normal $\mathbf{m}^{(s)}$ and the slip direction $\mathbf{s}^{(s)}$ of each slip system of the crystalline matrix are coplanar to the axes a_1 and a_2 of the voids, and hence can take the following forms

$$\mathbf{m}^{(s)} = \cos\theta^{(s)}\mathbf{e}_1 + \sin\theta^{(s)}\mathbf{e}_2,\ \ \mathbf{s}^{(s)} = -\sin\theta^{(s)}\mathbf{e}_1 + \cos\theta^{(s)}\mathbf{e}_2,\ \ \forall s = 1,\dots,K, \tag{2.6}$$

where $\theta^{(s)}$ are in-plane Euler angles as shown in Fig. 1. When the crystal is subjected to a stress $\boldsymbol{\sigma}$, the resolved shear stress acting on the sth slip system is given by $\tau^{(s)} = \boldsymbol{\sigma}\cdot\boldsymbol{\mu}^{(s)}$, while the strain-rate $\boldsymbol{D}$ in the crystal is assumed to be given by the superposition of the slip-rates of each slip system, i.e. $\boldsymbol{D} = \sum_{s=1}^{K}\gamma^{(s)}\boldsymbol{\mu}^{(s)}$. The slip-rate $\gamma^{(s)}$ is assumed to depend on the resolved shear stress $\tau^{(s)}$, via a slip potential $\Psi^{(s)}$ in such a way that

$$\gamma^{(s)} = \frac{\partial\Psi^{(s)}}{\partial\tau^{(s)}}\left(\tau^{(s)}\right). \tag{2.7}$$

The slip potentials $\Psi^{(s)}$ are assumed to be convex, incompressible and expressed via the power-law form

$$\Psi^{(s)}(\tau) = \frac{(\dot\gamma_0)^{(s)}(\tau_0)^{(s)}}{n+1}\left(\frac{|\tau|}{(\tau_0)^{(s)}}\right)^{n+1}. \tag{2.8}$$

Here, $n \geqslant 1$, $(\dot\gamma_0)^{(s)}$ and $(\tau_0)^{(s)}$ denote the creep exponent, the reference slip-rate and the reference flow stress (also denoted critical resolved shear stress CRSS) of the sth slip system, respectively. In addition, let us notice that the limiting values of the exponent, $n = 1$ and $n \to \infty$ correspond to linear viscoelasticicty and rate-independent perfect plasticity, respectively. In this connection, it is recalled that, even though the slip potentials $\Psi^{(s)}$ are not differentiable in the perfect crystal plasticity case, it is still possible to relate $\gamma^{(s)}$ and $\tau^{(s)}$ via the subdifferential of convex analysis.

Adding up the potentials of all the slip systems we obtain the constitutive behavior of the matrix phase, characterized by the viscoplastic stress potential U such that

$$U(\boldsymbol{\sigma}) = \sum_{s=1}^{K}\Psi^{(s)}(\tau^{(s)}) = \sum_{s=1}^{K}\frac{(\dot\gamma_0)^{(s)}(\tau_0)^{(s)}}{n+1}\left(\frac{|\tau^{(s)}|}{(\tau_0)^{(s)}}\right)^{n+1}. \tag{2.9}$$

Note that, in this last expression, U is a homogeneous function of degree $n+1$ in the stress $\boldsymbol{\sigma}$.

The corresponding Cauchy stress $\boldsymbol{\sigma}$ and the Eulerian strain-rate $\boldsymbol{D}$ in the matrix are related through the constitutive relation

$$\boldsymbol{D} = \frac{\partial U}{\partial\boldsymbol{\sigma}}(\boldsymbol{\sigma}). \tag{2.10}$$

2.4. The limit of infinite equiangular slip systems

In the following, we consider K equiangular slip systems by orientation angles $\theta^{(s)}$ equally partitioned in the interval $(-\pi/2, \pi/2)$, with K being the number of slip systems and $s = 1, K$ (see for instance Table 1).

Next, we consider the special, albeit very common, case of identical CRSS and reference slip-rate such that

$$(\tau_0)^{(s)} = \tau_0, \quad (\dot\gamma_0)^{(s)} = \dot\gamma_0, \quad \forall s = 1, K. \tag{2.11}$$

This analysis will be shown to be of critical importance in the following sections.

As a consequence of the plane-strain conditions, the resolved shear of each slip system is then written as

$$\begin{aligned}\tau^{(s)} &= \boldsymbol{\sigma}\cdot\boldsymbol{\mu}^{(s)} = \left(\frac{\sigma_{11}-\sigma_{22}}{2}\right)\sin 2\theta^{(s)} + \sigma_{12}\cos 2\theta^{(s)} \\ &= \frac{\sigma_{eq}}{\sqrt{3}}\sin\left(2\theta^{(s)} + \delta\right), \quad \forall s = 1, K\end{aligned} \tag{2.12}$$

with $\delta = \arctan\left(2\sigma_{12}/(\sigma_{11}-\sigma_{22})\right)$. By introducing this relation in Eq. (2.9), the viscoplastic stress potential U becomes

$$U(\boldsymbol{\sigma}) = \frac{\dot\gamma_0\tau_0}{n+1}\left(\frac{\sigma_{eq}}{\tau_0\sqrt{3}}\right)^{n+1}\sum_{s=1}^{K}\left|\sin\left(2\theta^{(s)} + \delta\right)\right|^{n+1}. \tag{2.13}$$

In the limit $K \longrightarrow \infty$, the matrix becomes isotropic and this leads to the following isotropic potential (see detailed proof in Appendix A)

$$U(\boldsymbol{\sigma}) \cong \frac{\dot\gamma_0\tau_0}{n+1}\left(\frac{\sigma_{eq}}{\tau_0\sqrt{3}}\right)^{n+1}\beta_n K, \quad \beta_n = \frac{2}{(n+1)\sqrt{\pi}}\frac{\Gamma\left(\frac{n+2}{2}\right)}{\Gamma\left(\frac{n+1}{2}\right)}, \tag{2.14}$$

where Γ is the Γ-function.

Finally, one can recover the constitutive behavior of an isotropic matrix phase, characterized by its viscoplastic stress potential

$$U(\boldsymbol{\sigma}) = \frac{\dot\epsilon_0\sigma_0}{n+1}\left(\frac{\sigma_{eq}}{\sigma_0}\right)^{n+1} \tag{2.15}$$

with $\dot\epsilon_0$ denoting the reference strain-rate, and σ_0 the isotropic flow stress by setting

$$\dot\gamma_0\tau_0^{-n}\left(\frac{1}{\sqrt{3}}\right)^{n+1}\beta_n K = \dot\epsilon_0\sigma_0^{-n}. \tag{2.16}$$

2.5. Gauge surface

For later use, it is convenient to define here the notion of the gauge surface. Gauge surfaces are equipotential surfaces which have a physical importance in the present analysis as they characterize the domain of statically admissible stresses and are analogous to the yield surfaces in rate-independent plasticity.

Using the homogeneity of the stress potential (2.9) for single crystal matrix together with the general definition of the effective stress behavior (2.2), one can show that the effective stress potential $\widetilde{U}$ is also homogeneous of degree $n+1$ in $\overline{\boldsymbol{\sigma}}$.

Table 1
Set of angles $\theta^{(s)}$ in several cases of equiangular slip systems.

$K=3$	$K=4$	$K=5$
$\theta^{(s)}=\{0,\pm\pi/3\}$	$\theta^{(s)}=\{0,\pm\pi/4,\pi/2\}$	$\theta^{(s)}=\{0,\pm\pi/5,\pm2\pi/5\}$

Therefore, it is convenient to introduce the so-called gauge surface P_n (the subscript being used to denote the dependence on the creep exponent n) as in Leblond et al. (1994). More precisely, it is sufficient to study only one of the equi-potential surfaces $\left\{\overline{\boldsymbol{\sigma}}, \widetilde{U}(\overline{\boldsymbol{\sigma}})=const\right\}$ i.e., the so-called gauge surface P_n of the porous material. For instance, in the case of slip systems with identical CRSS τ_0 and reference slip-rate $\dot{\gamma}_0$, one can define the equi-potential surfaces

$$P_n \equiv \left\{\overline{\boldsymbol{\Sigma}},\ \widetilde{U}(\overline{\boldsymbol{\Sigma}}, s_\alpha)=\frac{\dot{\gamma}_0\tau_0^{-n}}{n+1}\right\}. \tag{2.17}$$

Then, the gauge function $\widetilde{\Phi}_n$ provides the equation for the gauge surface via the expression

$$\overline{\boldsymbol{\Sigma}}\in P_n \Longleftrightarrow \widetilde{\Phi}_n(\overline{\boldsymbol{\Sigma}}, s_\alpha)=(n+1)\widetilde{U}(\overline{\boldsymbol{\Sigma}}, s_\alpha)-\dot{\gamma}_0\tau_0^{-n}=0. \tag{2.18}$$

The subscript n has been used to indicate that the gauge function depends explicitly on the creep exponent of the single crystal matrix. The above definitions of the gauge surface and gauge function are analogous to the well known yield function and yield surface in the context of rate-independent plasticity ($n\to\infty$).

3. Analytical homogenization model for the porous single crystal

3.1. The variational method

In the present work, we will make use of the general, nonlinear homogenization methods developed by Ponte Castañeda (1991a) and Ponte Castañeda (2002), which are based on the construction of a linear comparison composite (LCC) with the same microstructure as the nonlinear composite. More precisely, the different phases of the LCC are determined through well defined linearizations of the given nonlinear phases by making use of a suitably designed variational principle. The corresponding phases of the LCC are characterized in general by quadratic stress potentials of the form

$$U_L^{(r)}(\boldsymbol{\sigma}, \mathbf{S}^{(r)})=\frac{1}{2}\boldsymbol{\sigma}(\mathbf{x})\cdot\mathbf{S}^{(r)}\cdot\boldsymbol{\sigma}(\mathbf{x}),\quad r=1,2,\quad \forall\mathbf{x}\in\Omega^{(r)}, \tag{3.1}$$

where $\mathbf{S}^{(r)}$ serves to denote the fourth-order symmetric compliance tensor. In addition, as proposed by Ponte Castañeda (1991a, 2002), "corrector" functions $v^{(r)}$ can be defined as the optimal difference between the quadratic stress potentials and the actual nonlinear ones $U^{(r)}$ defined in (2.9), via

$$v^{(r)}(\mathbf{S}^{(r)})=\sup_{\widehat{\boldsymbol{\sigma}}^{(r)}}\left(U_L^{(r)}(\widehat{\boldsymbol{\sigma}}, \mathbf{S}^{(r)})-U^{(r)}(\widehat{\boldsymbol{\sigma}})\right). \tag{3.2}$$

Here, $\widehat{\boldsymbol{\sigma}}^{(r)}$ are assumed to be constant second-order tensors. For simplicity in notation, we precise that $\widehat{\boldsymbol{\sigma}}^{(r)}$ is the field that attains the "sup" operator in (3.2).

In the following, using (3.1) and (3.2), one can show that the effective energy function (2.2) can be approximated (Ponte Castañeda, 1991a, 2002) via the expression

$$\widetilde{U}_{var}(\overline{\boldsymbol{\sigma}})=\sup_{\mathbf{S}^{(r)}(x)}\left(\widetilde{U}_L(\overline{\boldsymbol{\sigma}}, \mathbf{S}^{(r)})-\sum_{r=1}^{2}c^{(r)}v^{(r)}\left(\mathbf{S}^{(r)}\right)\right), \tag{3.3}$$

where $c^{(r)}$ is the volume fraction of the phase r. It is interesting to note that Eq. (3.3) is a lower bound of the effective energy $\widetilde{U}(\overline{\boldsymbol{\sigma}})$. Nonetheless, the goal of the present work is to provide an estimate of $\widetilde{U}(\overline{\boldsymbol{\sigma}})$ and not a bound, thus, the optimization conditions on $\mathbf{S}^{(r)}$ will be further relaxed next.

3.2. Definition of a linear comparison composite

In this section, we choose the compliance tensors $\mathbf{S}^{(r)}$ in such a way that will allow us to get explicit estimates for $\widetilde{U}(\overline{\boldsymbol{\sigma}})$. The difficulty in the choice $\mathbf{S}^{(r)}$ is twofold. First, $\mathbf{S}^{(r)}$ do not need to be constant per phase (see Herve and Zaoui, 1993). While such a choice would lead to more accurate estimates, in general, one would have to resolve the fully numerical optimization of the problem. This makes it implicit and untractable in real applications. The second point is that one can choose piecewise constant but the most general form of $\mathbf{S}^{(r)}$ (see deBotton and Ponte Castañeda, 1995; Idiart and Ponte Castañeda, 2007). This choice again leads to a convex but sub-differentiable optimization problem for $\widetilde{U}(\overline{\boldsymbol{\sigma}})$ as a function of $\mathbf{S}^{(r)}$ and thus one has to resolve again the fully numerical optimization problem (except in special cases as in Idiart and Ponte Castañeda, 2007). For this reason, in the present work, we choose not only piecewise constant $\mathbf{S}^{(r)}$, but also of a special form which is motivated by the viscoplastic stress potential U in the linear case $n=1$. Motivated by (2.9) for $n=1$, we propose a linear viscoelastic potential of the form

$$U_L(\boldsymbol{\sigma})=\frac{1}{2}\boldsymbol{\sigma}\cdot\mathbf{S}_0\cdot\boldsymbol{\sigma}, \tag{3.4}$$

where $\mathbf{S}_0$ is a symmetric fourth-order compliance tensor for the LCC which reads

$$\begin{aligned}&\mathbf{S}_0=\sum_{s=1}^{K}\frac{1}{2\lambda^{(s)}}\mathbf{E}^{(s)}+\sum_{s=1}^{K}\frac{1}{2\rho^{(s)}}\mathbf{F}^{(s)}+\frac{1}{3\kappa}\mathbf{J},\\ &\mathbf{E}^{(s)}=2\boldsymbol{\mu}^{(s)}\otimes\boldsymbol{\mu}^{(s)},\quad \mathbf{F}^{(s)}=\mathbf{K}-\mathbf{E}^{(s)},\quad \forall s=1,K.\end{aligned} \tag{3.5}$$

Here $\mathbf{K}$ and $\mathbf{J}$ denote the fourth-order shear and hydrostatic projection tensors, respectively. Thus, for each $s=1,K$, the triplet $\left(\mathbf{E}^{(s)},\ \mathbf{F}^{(s)},\ \mathbf{J}\right)$ forms a fourth-order tensor basis.[1]

In addition, $\boldsymbol{\mu}^{(s)}$ is the Schmid tensor (2.5) associated to the s^{th} slip system. If one lets $\rho^{(s)}\to\infty$ and $\kappa\to\infty$ (incompressible matrix), then we recover the original linear viscoelastic potential, $U_L(\boldsymbol{\sigma})$ in Eq. (2.9), i.e.

$$U_L(\boldsymbol{\sigma})=\sum_{s=1}^{K}\frac{(\gamma_0)^{(s)}}{2(\tau_0)^{(s)}}\left(\tau^{(s)}\right)^2,\quad \tau^{(s)}=\sqrt{\frac{\boldsymbol{\sigma}\cdot\mathbf{E}^{(s)}\cdot\boldsymbol{\sigma}}{2}}. \tag{3.6}$$

The reason for using the more general form (3.5) instead of $\mathbf{S}_0=\sum_{s=1}^{K}\frac{1}{2\lambda^{(s)}}\mathbf{E}^{(s)}$ is for later non-singular evaluation of the Hill-Eshelby tensor as discussed in the following.

Using the generalized (Hashin and Shtrikman, 1963) estimates of Willis (1977), which are known to be quite accurate for low-to-moderate random distributions of voids, one gets

$$\widetilde{U}_L(\overline{\boldsymbol{\sigma}})=\frac{1}{2(1-f)}\overline{\boldsymbol{\sigma}}\cdot\left(\sum_{s=1}^{K}\frac{1}{2\lambda^{(s)}}\mathbf{E}^{(s)}+f\mathbf{S}_0^{*}\right)\cdot\overline{\boldsymbol{\sigma}}, \tag{3.7}$$

where

$$\mathbf{S}_0^{*}\left(\lambda^{(s)}\right)=\lim_{\rho^{(s)},\kappa\to\infty}\mathbf{Q}^{-1}\left(\lambda^{(s)}\right)-\sum_{s=1}^{K}\frac{1}{2\lambda^{(s)}}\mathbf{E}^{(s)},\quad \mathbf{Q}=\mathbf{L}_0-\mathbf{L}_0\mathbf{P}\mathbf{L}_0. \tag{3.8}$$

[1] $\mathbf{F}^{(s)}\cdot\mathbf{F}^{(s)}=\mathbf{F}^{(s)},\ \mathbf{E}^{(s)}\cdot\mathbf{E}^{(s)}=\mathbf{E}^{(s)},\ \mathbf{E}^{(s)}\cdot\mathbf{F}^{(s)}=\mathbf{F}^{(s)}\cdot\mathbf{E}^{(s)}=0,\ \forall s=1,K.$

In this relation, $\mathbf{Q}$ is a fourth-order microstructural tensor given in terms of the elasticity tensor $\mathbf{L}_0 = \mathbf{S}_0^{-1}$, and the (Eshelby, 1957) tensor $\mathbf{P}$.

For cylindrical voids with elliptical cross-section (i.e., aspect ratio $w \neq 1$) embedded in a matrix with elasticity $\mathbf{L}_0$, the Eshelby tensor $\mathbf{P}$ reads

$$\mathbf{P}_{ijkl} = \frac{w}{2\pi}\int_0^{2\pi} \frac{\left(L_{iakb}\xi_a\xi_b\right)^{-1}\xi_j\xi_l|_{(ij)(kl)}}{\xi\cdot\left(\boldsymbol{Z}^T\boldsymbol{Z}\right)^{-1}\cdot\xi}d\phi \tag{3.9}$$

where the brackets $(ij)(kl)$ denote symmetrization with respect to the corresponding indices, $\xi = \{\cos\phi, \sin\phi\}$ is the position vector and $\boldsymbol{Z}$ the shape tensor expressed as

$$\boldsymbol{Z} = \mathbf{n}^{(1)}\otimes\mathbf{n}^{(1)} + \frac{1}{w}\mathbf{n}^{(2)}\otimes\mathbf{n}^{(2)}. \tag{3.10}$$

It is recalled here that w and $\mathbf{n}^{(i)}$ have been defined in the context of Fig. 1.

At this point it is important to note that after the limit of $\rho^{(s)} \to \infty$ and $\kappa \to \infty$ are considered in (3.8) the $\mathbf{Q}$ tensor is compressible due to the presence of the voids in the matrix. These limits need to be taken during the evaluation of $\mathbf{Q}$ in (3.8_2). If instead the limit is taken before the evaluation of $\mathbf{Q}$ the term $L_{iakb}\xi_a\xi_b$ in (3.9) becomes singular.

The computation of $\mathbf{Q}$ in the above expressions is critical for the optimization problem (3.3). Due to the extremely complicated dependence of $\mathbf{Q}$ on $\lambda^{(s)}$, the optimization problem for the estimation of the effective response in Eq. (3.3) has to be carried out numerically, except in the special case where we let $\lambda^{(s)} \to \lambda$ for all $s = 1, K$. This simplifies tremendously the evaluation of the $\mathbf{Q}$ tensor and allows for approximations as is discussed in the following section.

More specifically, one can write

$$\lim_{\lambda^{(s)}\to\lambda}\mathbf{S}_0^*\left(\lambda^{(s)}\right) = \frac{1}{\lambda}\widehat{\mathbf{S}}_0^*, \tag{3.11}$$

where $\widehat{\mathbf{S}}_0^*$ is given by (c.f. (3.8))

$$\widehat{\mathbf{S}}_0^* = \widehat{\mathbf{Q}}^{-1} - \sum_{s=1}^{K}\frac{1}{2}\mathbf{E}^{(s)}, \quad \widehat{\mathbf{Q}}^{-1} = \lambda\lim_{\lambda^{(s)}\to\lambda}\mathbf{Q}^{-1}\left(\lambda^{(s)}\right). \tag{3.12}$$

It is very important to stress at this point that the tensors $\widehat{\mathbf{Q}}$ and consequently $\widehat{\mathbf{S}}_0^*$ in the above expression are independent of λ (see relevant discussion in Danas (2008) and Danas and Ponte Castañeda (2009a)). This property will allow to carry out analytically the optimization problem (3.3) to be discussed in detail in the next section.

But before proceeding to that, we first provide analytical expressions for the microstructural tensor $\widehat{\mathbf{S}}_0^*$, which reads

$$\widehat{\mathbf{S}}_0^* = \frac{1}{2w\sqrt{2}}\sqrt{\sum_{j\neq l}\left(1-\cos 4\left(\theta^{(j)}-\theta^{(l)}\right)\right)}\mathbf{G}, \tag{3.13}$$

where the components of tensor $\mathbf{G}$ are given by

$$\mathbf{G}_{1111} = w^2\cos^2\psi + \sin^2\psi, \quad \mathbf{G}_{1122} = 0, \quad \mathbf{G}_{1112} = \frac{1}{4}\left(w^2-1\right)\sin 2\psi,$$
$$\mathbf{G}_{2222} = \cos^2\psi + w^2\sin^2\psi, \quad \mathbf{G}_{2212} = \mathbf{G}_{1112}, \quad \mathbf{G}_{1212} = \frac{1}{4}\left(1+w^2\right). \tag{3.14}$$

It should be mentioned here that $\mathbf{G}$ possesses both major and minor symmetry, and has a similar form to that obtained for an isotropic matrix comprising elliptical voids (see Danas, 2008).

3.3. Variational estimate for porous single crystal

Using the above definition (3.4), (3.5) and the estimate (3.7), one can rewrite the nonlinear effective potential $\widetilde{U}$, defined in (3.3) as

$$\widetilde{U}_{var}(\overline{\boldsymbol{\sigma}}) = \max_{\lambda^{(s)}\geqslant 0}\left(\widetilde{U}_L(\overline{\boldsymbol{\sigma}}) - (1-f)\sum_{s=1}^{K}v^{(s)}\left(\lambda^{(s)}\right)\right). \tag{3.15}$$

For $n > 1$, the corrector function for a single slip system can be expressed analytically (deBotton and Ponte Castañeda, 1995) as

$$v^{(s)}\left(\lambda^{(s)}\right) = \max_{\widehat{\tau}^{(s)}\geqslant 0}\left(\frac{1}{2\lambda^{(s)}}\left(\widehat{\tau}^{(s)}\right)^2 - \Psi^{(s)}\left(\widehat{\tau}^{(s)}\right)\right)$$
$$= \frac{n-1}{n+1}\frac{\left(\dot{\gamma}_0\right)^{(s)}\left(\tau_0\right)^{(s)}}{2}\left(\frac{\left(\tau_0\right)^{(s)}}{\lambda^{(s)}\left(\dot{\gamma}_0\right)^{(s)}}\right)^{\frac{(n+1)}{(n-1)}}. \tag{3.16}$$

The global optimization problem in (3.15) is a non-trivial one, mainly because of the extremely complicated dependence of the $\mathbf{Q}$ tensor (see (3.8)) on $\lambda^{(s)}$, and in general, it must be carried out numerically. However, we introduce at this point the approximation

$$\mathbf{S}_0^*\left(\lambda^{(s)}\right) \cong \frac{1}{K}\sum_{s=1}^{K}\frac{1}{\lambda^{(s)}}\widehat{\mathbf{S}}_0^*, \tag{3.17}$$

where $\widehat{\mathbf{S}}_0^*$ is given by (3.12). This last expression (3.17) is identically true for $\lambda^{(s)} = \lambda$, $\forall s = 1, K$ while being a relatively good approximation in the neighborhood of $\lambda^{(i)} \simeq \lambda^{(j)}$, $\forall i, j = 1, K$. The choice (3.17) allows for a fully analytical resolution of the optimization procedure (3.15) and thus to a fully analytical model.

Consequently, the relation (3.17) together with Eqs. (3.7), (3.15) and (3.16) lead to

$$\widetilde{U}_{var}(\overline{\boldsymbol{\sigma}}) = max_{\lambda^{(s)}\geqslant 0}\left[\sum_{s=1}^{K}\left\{\frac{1}{1-f}\frac{1}{2\lambda^{(s)}}\left(\left(\tau^{(s)}\right)^2 + \frac{f}{K}\overline{\boldsymbol{\sigma}}\cdot\widehat{\mathbf{S}}_0^*\cdot\overline{\boldsymbol{\sigma}}\right)\right\}\right.$$
$$\left. - (1-f)\sum_{s=1}^{K}\frac{n-1}{n+1}\frac{\left(\dot{\gamma}_0\right)^{(s)}\left(\tau_0\right)^{(s)}}{2}\left(\frac{\left(\tau_0\right)^{(s)}}{\lambda^{(s)}\left(\dot{\gamma}_0\right)^{(s)}}\right)^{\frac{(n+1)}{(n-1)}}\right]. \tag{3.18}$$

Following Han et al. (2013), we interchange the maximization with the summation in (3.18) to get

$$\frac{1}{2\lambda^{(s)}} = \frac{\left(\dot{\gamma}_0\right)^{(s)}}{2\left(\tau_0\right)^{(s)}}\left\{\frac{\left(\tau^{(s)}\right)^2 + \frac{f}{K}\overline{\boldsymbol{\sigma}}\cdot\widehat{\mathbf{S}}_0^*\cdot\overline{\boldsymbol{\sigma}}}{\left(\left(\tau_0\right)^{(s)}\right)^2(1-f)^2}\right\}^{(n-1)/2} \tag{3.19}$$

This interchange will preserve the discrete character of the slip-system response in the rate-independent limit and for $f = 0$.

Finally, substitution of (3.19) to (3.15) gives the variational estimate of the effective stress potential of the crystalline porous material

$$\widetilde{U}_{var}(\overline{\boldsymbol{\sigma}}) = (1-f)^{-n}\sum_{s=1}^{K}\frac{\left(\dot{\gamma}_0\right)^{(s)}\left(\tau_0\right)^{(s)}}{n+1}\left(\frac{\left|\widetilde{\tau}^{(s)}\right|}{\left(\tau_0\right)^{(s)}}\right)^{n+1},$$
$$\widetilde{\tau}^{(s)} = \sqrt{\left(\tau^{(s)}\right)^2 + \frac{f}{K}\overline{\boldsymbol{\sigma}}\cdot\widehat{\mathbf{S}}_0^*\cdot\overline{\boldsymbol{\sigma}}}, \tag{3.20}$$

which can also be written as

$$\widetilde{U}_{var}(\overline{\boldsymbol{\sigma}}) = (1-f)^{-n}\sum_{s=1}^{K}\frac{\left(\dot{\gamma}_0\right)^{(s)}\left(\left(\tau_0\right)^{(s)}\right)^{-n}}{n+1}\left(\overline{\boldsymbol{\sigma}}\cdot\widehat{\mathbf{S}}^{var,(s)}\cdot\overline{\boldsymbol{\sigma}}\right)^{(n+1)/2} \tag{3.21}$$

with

$$\widehat{\mathbf{S}}^{var,(s)} = \frac{1}{2}\mathbf{E}^{(s)} + \frac{f}{K}\widehat{\mathbf{S}}_0^*, \quad \forall s = 1, K. \tag{3.22}$$

It is recalled that $\widehat{\mathbf{S}}_0^*$ is given by Eq. (3.13)

3.4. Correction of the hydrostatic point

In this subsection, we introduce a correction to the $\widetilde{U}_{var}$ estimate (3.21) in the limit of purely hydrostatic loadings. It is well known from Ponte Castañeda (1991b) and Michel and Suquet (1992) that in the case of isotropic matrix and hydrostatic loadings the variational estimates are overly stiff. This is also the case in the present work, i.e. the estimate (3.21) for $\widetilde{U}_{var}$ is also very stiff when compared to numerical unit-cell calculations.

The way to remedy this overly stiff response is to use the fact that in the isotropic case, the hydrostatic limit of the effective behavior of composite cylinder assemblages (CCA) is known exactly and in closed form (Hashin, 1962; Gurson, 1977; Leblond et al., 1994) and can be expressed as

$$\frac{\overline{\sigma}_m}{\sigma_0} = n\left(f^{-1/n}-1\right)\cdot\frac{1}{3^{\frac{n+1}{2n}}}\cdot\left(\frac{2\overline{D}_m}{\dot{\epsilon}_0}\right)^{1/n}. \tag{3.23}$$

In the present case of anisotropic crystal plasticity no simple analytic solution is available similar to the one in (3.23). Nevertheless, one can insist that the estimate (3.21) should recover the result (3.23) in the limit of infinite equiangular slip systems, circular voids and hydrostatic loadings, where the response becomes fully isotropic.

To achieve this goal and motivated by similar work on isotropic matrix systems (Danas and Aravas, 2012 but see also Danas et al., 2008), we propose the following modification in (3.21)

$$\widetilde{U}_{mvar}(\overline{\boldsymbol{\sigma}}) = (1-f)^{-n}\sum_{s=1}^{K}\frac{(\dot{\gamma}_0)^{(s)}\left((\tau_0)^{(s)}\right)^{-n}}{n+1}\left(\overline{\boldsymbol{\sigma}}\cdot\widehat{\mathbf{S}}^{mvar,(s)}\cdot\overline{\boldsymbol{\sigma}}\right)^{(n+1)/2},$$
$$\widehat{\mathbf{S}}^{mvar,(s)} = \widehat{\mathbf{S}}^{var,(s)} + \left(q_J^2-1\right)\mathbf{J}\cdot\widehat{\mathbf{S}}^{var,(s)}\cdot\mathbf{J}. \tag{3.24}$$

The label "mvar" refers to "modified variational" (MVAR), whereas the factor "q_J" remains to be defined so that we obtain the CCA result (3.23) in the limit $K\longrightarrow\infty$.

In this connection, we consider a purely hydrostatic loading $\overline{\boldsymbol{\sigma}}_{ij}=\overline{\sigma}_m\delta_{ij}$ and circular voids (i.e., $w=1$) embedded in a single crystal comprising slip systems with identical CRSS and reference slip rate, i.e. $(\tau_0)^{(s)}=\tau_0,\ (\dot{\gamma}_0)^{(s)}=\dot{\gamma}_0,\ \forall s=1,K$. In the case of infinite and/or equiangular slip systems, we can write (see relations (3.32) and (B.3) where $w=1$)

$$\widehat{\mathbf{S}}^{(s)} = \frac{1}{2}\mathbf{E}^{(s)}+\frac{f}{4}\mathbf{I},\quad \forall s=1,K\ \Rightarrow\ \widetilde{U}_{mvar}(\overline{\boldsymbol{\sigma}})$$
$$= (1-f)^{-n}K\frac{\dot{\gamma}_0\tau_0^{-n}}{n+1}\overline{\sigma}_m^{n+1}\left(\frac{f}{2}q_J^2\right)^{\frac{n+1}{2}}. \tag{3.25}$$

Thus, by using relations (2.4), (2.16), (3.24) and (3.25), one obtains the correction for q_J to be

$$q_J = \sqrt{\frac{2}{f}}\left\{\frac{(1-f)(\beta_n)^{\frac{1}{n}}}{n(f^{-1/n}-1)}\right\}^{\frac{n}{n+1}}, \tag{3.26}$$

where β_n is given by expression (2.14).

3.5. Summary of the modified variational model (MVAR)

Thus the main result of the present paper can be summarized as follows

$$\widetilde{U}_{mvar}(\overline{\boldsymbol{\sigma}}) = (1-f)^{-n}\sum_{s=1}^{K}\frac{(\dot{\gamma}_0)^{(s)}\left((\tau_0)^{(s)}\right)^{-n}}{n+1}\left(\overline{\boldsymbol{\sigma}}\cdot\widehat{\mathbf{S}}^{(s)}\cdot\overline{\boldsymbol{\sigma}}\right)^{(n+1)/2}, \tag{3.27}$$

where

$$\widehat{\mathbf{S}}^{(s)} \equiv \widehat{\mathbf{S}}^{mvar,(s)} = \widehat{\mathbf{S}}^{var,(s)} + \left(q_J^2-1\right)\mathbf{J}\cdot\widehat{\mathbf{S}}^{var,(s)}\cdot\mathbf{J} \tag{3.28}$$

and

$$\widehat{\mathbf{S}}^{var,(s)} = \frac{1}{2}\mathbf{E}^{(s)}+\frac{f}{2Kw\sqrt{2}}\sqrt{\sum_{j\neq l}\left(1-\cos 4\left(\theta^{(j)}-\theta^{(l)}\right)\right)}\mathbf{G},\quad \forall s=1,K. \tag{3.29}$$

The components of tensor $\mathbf{G}$ are given by Eq. (3.14) and are repeated here for completeness

$$\mathbf{G}_{1111} = w^2\cos^2\psi+\sin^2\psi,\ \ \mathbf{G}_{1122}=0,\ \ \mathbf{G}_{1112}=\frac{1}{4}(w^2-1)\sin 2\psi,$$
$$\mathbf{G}_{2222} = \cos^2\psi+w^2\sin^2\psi,\ \ \mathbf{G}_{2212}=\mathbf{G}_{1112},\ \ \mathbf{G}_{1212}=\frac{1}{4}(1+w^2). \tag{3.30}$$

In addition, q and β_n are

$$q_J = \sqrt{\frac{2}{f}}\left\{\frac{(1-f)(\beta_n)^{\frac{1}{n}}}{n(f^{-1/n}-1)}\right\}^{\frac{n}{n+1}},\quad \beta_n = \frac{2}{(n+1)\sqrt{\pi}}\frac{\Gamma\left(\frac{n+2}{2}\right)}{\Gamma\left(\frac{n+1}{2}\right)} \tag{3.31}$$

with Γ being the Γ-function.

Two special cases of interest can be further spelled out here. First, the special case of circular voids leads to $\mathbf{G}=\mathbf{I}=\mathbf{K}+\mathbf{J}$ through the relation (3.14). This implies that the purely hydrostatic part of $\widehat{\mathbf{S}}^{var,(s)}$ in Eq. (3.29) depends strongly on both the number of slip systems K as well as on their orientation angles $\theta^{(s)}$. This effect is discussed in detail later in the results sections.

Second, if we consider a single crystal with "equiangular slip systems", as shown in Table 1, one gets

$$\sqrt{\sum_{j\neq l}\left(1-\cos 4\left(\theta^{(j)}-\theta^{(l)}\right)\right)} = \frac{K}{\sqrt{2}},\quad \Rightarrow \widehat{\mathbf{S}}^{var,(s)} = \frac{1}{2}\mathbf{E}^{(s)}+\frac{f}{4w}\mathbf{G}. \tag{3.32}$$

In the following, we present a numerical homogenization analysis which will serve to assess the accuracy of the proposed homogenization model.

4. Numerical homogenization

Numerical techniques (e.g. finite element method) are able, in principle, to solve for the local field in a porous material, provided that the exact location and distribution of the pores is known. Nevertheless, in most cases of interest, the only available information is the void volume fraction (or porosity) and, possibly, the two-point probability distribution function of the voids (i.e., isotropic, orthotropic, etc). Moreover, for sufficient accuracy the element size that should be used in a finite element program must be much smaller than the size of the voids, which in turn is smaller than the size of the periodic unit-cell, especially when multiple pores are considered. This makes the computation very intensive in time. Due to all these reasons, it is very difficult to use the numerical results in a multi-scale analysis, especially when the unit-cell is rather complex.

Nonetheless, one could use the numerical periodic homogenization technique as rigorous test-bed to assess the simpler analytical models as the one proposed in the previous section. More precisely, we can analyze the problem of a periodic porous material considering a unit-cell that contains a given distribution of voids. On the other hand, it is well known that a random porous material (e.g., the one in the analytical model presented in the previous section) and the periodic material exhibit similar effective behavior either in the case where the distribution of voids is complex enough (adequate for large porosity) or in the limiting case where

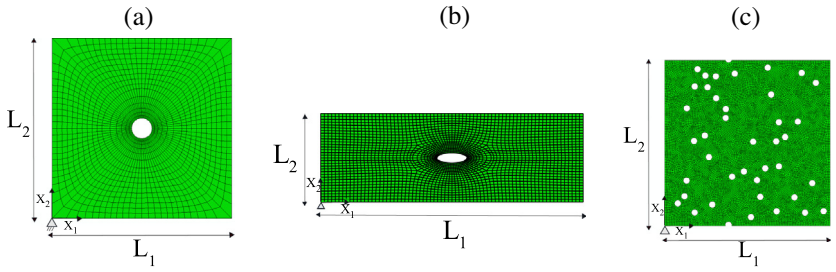

Fig. 2. Undeformed unit-cell "square" geometry in the case of (a) a single circular void (b) a distribution of several circular voids (c) a single elliptical void.

the porosity is small enough. Furthermore, in these cases, the periodic unit-cell estimates, and consequently the effective properties of the periodic composite, are independent of the prescribed periodic boundary conditions (Gilormini and Michel, 1998). In this regard then, the comparison between the proposed model and the FE periodic unit-cell calculations are meaningful provided that complex periodic geometries are considered or porosity is small.

The following FE calculations have been carried out with the commercial code Abaqus (2009) by use of a user-material subroutine for specific 2D crystal plasticity, based on the notes of Huang (1991) and Kysar (1997).

4.1. Unit-cell geometries and periodic boundary conditions

As already seen before, FE periodic unit-cell calculations need to be carried out in order to validate the model. Thus, different unit-cell geometries used in our computations, subjected to periodic boundary conditions, would be presented in this subsection. The present FE calculations are carried out using a small strain formulation since the scope of the study is the estimation of the effective response of the porous crystal with a given microstructural realization but not the evolution of microstructure which is left for a subsequent work. Moreover, it is important to notice that the entire unit-cell is considered here because there exist no planes of symmetry due to the coupling between the crystal anisotropy and the microstructure anisotropy except in few special cases such as circular voids and particular slip orientations.

4.1.1. Unit-cell geometries

In the case of small porosities ($f = 1\%$ in the present study), geometries with one void in the middle of the unit-cell can be used to estimate the effective behavior of the porous material. In order to achieve this goal, a unit-cell made up of a long cylindrical void with an initially circular (or even elliptical) cross-section in the plane 1–2 (see Fig. 2(a) and (b)) is considered. Moreover, plane-strain elements are used to simulate the x_3 direction.

On the other hand, for large porosities ($f = 5\%$ in the present study), one needs more complex distribution of voids, i.e. multi-pore geometries to achieve isotropic distributions. In this regard, we make use of monodisperse distributions (e.g. Fig. 2(c)) that are constructed by means of a random sequential adsorption algorithm (see Rintoul and Torquato, 1997; Torquato, 2002) which generates the coordinates of the pore centers. For monodisperse distributions, the radius of each void is

$$R_m = L\left(\frac{f}{\pi N}\right)^{1/2} \tag{4.1}$$

with N being the number of pores in the unit-cell and f the porosity.

In addition, the sequential addition of voids is constrained so that the distance between a given void and the rest of the voids as well as the boundaries of the unit-cell takes a minimum value that guaranties adequate spatial discretization. In order to achieve this we write down the following rules (Segurado and Llorca, 2002; Fritzen et al., 2012; López Jiménez and Pellegrino, 2012; Lopez-Pamies et al., 2013; López Jiménez, 2014).

- The center-to-center distance between a new pore i in the sequential algorithm and any previously generated pore $j = 1, \ldots, i-1$ has to exceed the minimum value fixed here as $s_1 = 2.04R_m$. If the surface of particle i cuts any of the unit-cell surfaces, this condition has to be checked with the pores near the opposite surface because the microstructure of the composite is periodic. Mathematically, these conditions can be expressed as

$$\|\mathbf{X}^i - \mathbf{X}^j - \mathbf{h}\| \geqslant s_1, \tag{4.2}$$

  where $\mathbf{X}^i\left(\mathbf{X}^j\right)$ denotes the location of the center of particle $i(j)$ and $\mathbf{h}$ is a vector with entries 0, L, or $-L$ where L is the dimension of the unit-cell.
- The void surface must be far enough from the unit-cell faces to prevent the occurrence of distorted finite element during meshing. This is expressed by the conditions

$$\left|X_k^i - R_m\right| \geqslant s_2 \quad \text{and} \quad \left|X_k^i + R_m - L\right| \geqslant s_2 \quad (k = 1, 2), \tag{4.3}$$

  where L is the length of the unit-cell s_2 has been fixed as $s_2 = 0.05R_m$.

Furthermore, periodic boundary conditions have to be applied to these geometries since the validation of the model requires periodic FE unit-cell calculations.

4.1.2. Periodic boundary conditions

The periodic boundary conditions are expressed in this case as (Michel et al., 1999; Miehe et al., 1999)

$$\mathbf{v}(\mathbf{x}) = \overline{\boldsymbol{D}} \cdot \mathbf{x} + \mathbf{v}^*(\mathbf{x}), \quad \mathbf{v}^* \text{ periodic}, \tag{4.4}$$

where the second-order tensor $\overline{\boldsymbol{D}}$ denotes the symmetric part of the average velocity gradient, $\mathbf{x}$ denotes the spatial coordinates and $\mathbf{v}^*$ is a periodic field.

Next, one needs to fix one node to cancel the rigid body motion in the FE calculations. For convenience, we choose this node to be at the origin such that $v_i(0,0) = 0$ $(i = 1, 2)$.

Subsequently, one can subtract the nodal velocities of opposite boundary sides (where $\mathbf{v}^*$ is equal) so that we get the following nodal constraints for the corner nodes, i.e.,

$$\begin{aligned} &v_i(L_1, 0) - v_i(0,0) = \overline{D}_{i1} L_1 = v_i(L_1, 0), \\ &v_i(0, L_2) - v_i(0,0) = \overline{D}_{i2} L_2 = v_i(0, L_2), \quad \forall i = 1, 2. \end{aligned} \tag{4.5}$$

The above simple relations show that the velocity components of the nodes $(L_1, 0)$ and $(0, L_2)$ are one-to-one connected to the symmetric part of the average velocity gradient $\overline{\boldsymbol{D}}$. Then, one can write

the constraint equations for the rest of the nodes making use of the result (4.5), i.e.,

$$\begin{aligned} &v_i(L_1,L_2) - v_i(0,L_2) = \overline{D}_{i1}L_1 = v_i(L_1,0),\\ &v_i(L_1,x_2) - v_i(0,x_2) = \overline{D}_{i1}L_1 = v_i(L_1,0),\\ &v_i(x_1,L_2) - v_i(x_1,0) = \overline{D}_{i2}L_2 = v_i(0,L_2), \quad \forall i = 1,2. \end{aligned} \tag{4.6}$$

The above algebraic analysis reveals that all periodic linear constraints between all nodes can be written in terms of the velocities of two corner nodes, i.e., $v_i(L_1,0)$ and $v_i(0,L_2)$, which, in turn, are given in terms of $\overline{\boldsymbol{D}}$ by Eq. (4.5). This, further, implies that the only nodes that boundary conditions need to be applied are $(L_1,0)$ and $(0,L_2)$ (together with the axes origin $(0,0)$ which is fixed).

In order, to validate the model proposed in this study, it is convenient to apply $\overline{\boldsymbol{D}}$ in such a way that the average stress triaxiality in the unit-cell remains constant.

4.2. Loading through stress triaxiality control

In this subsection, we will discuss the methodology for the application of a constant average stress triaxiality in the unit-cell. This methodology has been originally proposed by Barsoum and Faleskog (2007) and further discussed in Mbiakop et al. (2015).

Specifically, the applied load is such that the principal axes of the void do not rotate around the 3rd axis, and consequently the only non-zero components of the macroscopic stress tensor are

$$\overline{\boldsymbol{\sigma}} = \overline{\sigma}_{11}\,\mathbf{e}_1\otimes\mathbf{e}_1 + \overline{\sigma}_{22}\,\mathbf{e}_2\otimes\mathbf{e}_2, \tag{4.7}$$

As a consequence of above-defined load and the periodic boundary conditions, the average deformation in the unit-cell is entirely described by the displacements of the two corner nodes, e.g., $u_1(L_1,0) = U_1(t)$ and $u_2(0,L_2) = U_2(t)$, denoted compactly as

$$\mathbf{U} = \{U_1(t), U_2(t)\}, \quad \dot{U}v = \left\{\dot{U}_1(t), \dot{U}_2(t)\right\} \equiv \{v_1(t), v_2(t)\}. \tag{4.8}$$

Recalling that the average strain-rate and stress tensors involve only two non-zero components due to the applied triaxial loading, they can be expressed in vectorial form (i.e., using the Voigt notation) as

$$\overline{\boldsymbol{D}} = \left\{\frac{\dot{U}_1}{L_1+U_1}, \frac{\dot{U}_2}{L_2+U_2}\right\}, \quad \overline{\boldsymbol{\sigma}} = \{\overline{\sigma}_{11}, \overline{\sigma}_{22}\}. \tag{4.9}$$

To proceed further, we rewrite the strain-rate tensor as

$$\overline{\boldsymbol{D}} = \mathcal{Q}^{-1}\cdot\dot{\mathbf{U}}, \quad \mathcal{Q} = \mathrm{diag}(L_1+U_1, L_2+U_2). \tag{4.10}$$

We, next, define an external fictitious node,[2] whose generalized force, $\mathbf{P}_G$, and generalized displacement, $\mathbf{p}_G$, vectors, respectively, take the form $\mathbf{P}_G = \left\{P_1^G(t), 0\right\}$, $\mathbf{p}_G = \{p_1^G(t), p_2^G(t)\}$.

The stress state in the unit-cell is then controlled via a time-dependent kinematic constraint (Michel et al., 1999) obtained by equilibrating the rate of work in the unit-cell with the rate of work done by the fictitious node on the unit-cell at time t, such that

$$\dot{W} = S\overline{\boldsymbol{\sigma}}\cdot\overline{\boldsymbol{D}} = \mathbf{P}_G\cdot\dot{\mathbf{p}}_G. \tag{4.11}$$

Next, in order to control the loading path in the stress space, we couple the average stress $\overline{\boldsymbol{\sigma}}$ in the unit-cell with the generalized force vector associated with the fictitious node $\mathbf{P}_G$ via the constraint equation

$$S\overline{\boldsymbol{\sigma}} = \mathbf{C}\cdot\mathbf{P}_G, \quad \mathbf{C} = \left(\frac{\mathbf{c}_1}{|\mathbf{c}_1|}; \frac{\mathbf{c}_2}{|\mathbf{c}_2|}\right)^T, \quad \mathbf{C}^{-1} = \mathbf{C}^T, \tag{4.12}$$

[2] The fictitious node introduced in the present study has no specific physical interpretation, but serves only as a mathematical tool to apply the required boundary conditions at the unit-cell.

where $\mathbf{C}$ is a non-dimensional proper orthogonal matrix since $\mathbf{c}_i$ (i = 1,2) are two dimensional vectors that form an orthogonal basis set. The vectors $\mathbf{c}_i$ (i = 1,2) depend on the three components of the average stress $\overline{\boldsymbol{\sigma}}$, such that

$$\mathbf{c}_1 = \{\overline{\sigma}_{11}, \overline{\sigma}_{22}\}, \quad \mathbf{c}_2 = \{-\overline{\sigma}_{22}, \overline{\sigma}_{11}\}. \tag{4.13}$$

On the other hand, the principal components of the stress field can be expressed as a function of X_Σ, via

$$\frac{1}{\overline{\sigma}_{eq}}\{\overline{\sigma}_{11}, \overline{\sigma}_{22}\} = \frac{1}{\sqrt{3}}\{-1,1\} + X_\Sigma\{1,1\}, \tag{4.14}$$

where $\overline{\sigma}_{eq}$ denotes the equivalent Von Mises part of $\overline{\boldsymbol{\sigma}}$, and we set $\overline{\sigma}_{22} - \overline{\sigma}_{11} > 0$ since the gauge surface is symmetric with respect to the origin.

The above expressions for the vectors $\mathbf{c}_i$ (i = 1,2) together with the relation (4.14) further imply that the matrix $\mathbf{C}$ in Eq. (4.12) is only a function of the stress triaxiality X_Σ but not of the equivalent stress $\overline{\sigma}_{eq}$. By substitution of Eqs. (4.10) and (4.12) in (4.11), one gets

$$\dot{\mathbf{U}} = \mathcal{Q}\cdot\mathbf{C}\cdot\dot{\mathbf{p}}_G. \tag{4.15}$$

The above expression provides the kinematic constraints between the degrees of freedom corresponding to the sides of the unit-cell (i.e., $\mathbf{U}$) and the degrees of freedom of the fictitious node (i.e., $\mathbf{p}_G$). These nonlinear constraints are applied in the finite element software ABAQUS by use of the multi-point constraint user subroutine (MPC).

5. Results: Assessment of MVAR model via FE simulations

This section presents results for the effective behavior of rate-dependent porous single crystals as predicted by the modified variational model (MVAR) proposed in this work. The predictions of the MVAR are compared with corresponding results obtained by the FE simulations described in Section 4. Before proceeding with the discussion of the results, it is useful to introduce first the various material and loading parameters used in the following figures. The present study investigates a range of creep exponents $n = (1,2,5,10)$, porosities $f = (1\%, 5\%)$, void shapes and orientations (e.g., circular and elliptical) as well as a number of slip systems $K = (1,2,3,4,5,10)$ with various orientations.

Moreover, motivated by common practice in crystal plasticity studies, we consider the case where all the slip systems of the matrix have the same critical resolved shear stress (CRSS) and reference slip-rate, as defined in Eq. (2.11).

5.1. Computation of the gauge surface in the numerical homogenization

The evaluation of the gauge surfaces resulting from the numerical computations can be expressed using the definition (2.17) but its evaluation is non trivial and is described in the following. The general idea follows from the earlier study of Flandi and Leblond, 2005 but is rather different since it has to be appropriately modified to apply for the general commercial code Abaqus used in the present study.

By making use of the homogeneity of degree $n+1$ in $\overline{\boldsymbol{\Sigma}}$ of the function $\widetilde{U}$ (see (2.2)), one can write

$$\widetilde{U}(\overline{\boldsymbol{\Sigma}}) = \left(\overline{\Sigma}_{eq}\right)^{n+1}\widetilde{U}_N(\boldsymbol{N}, X_\Sigma) = \frac{\dot{\gamma}_0\tau_0^{-n}}{n+1}, \tag{5.1}$$

while $\boldsymbol{N} = \overline{\boldsymbol{\Sigma}}^d/\overline{\Sigma}_{eq}$ describes the loading direction in the deviatoric space, with $\overline{\boldsymbol{\Sigma}}^d$ and $\overline{\Sigma}_{eq}$ denoting the deviatoric and equivalent Von Mises part of the average stress $\overline{\boldsymbol{\Sigma}}$, respectively, corresponding to the equi-potential surface (2.17).

Next, given any average stress, $\overline{\boldsymbol{\sigma}}$, one can write

$$\widetilde{U}(\overline{\boldsymbol{\sigma}}) = (1-f)\min_{\boldsymbol{\sigma}\in S(\overline{\boldsymbol{\sigma}})}\langle U(\boldsymbol{\sigma})\rangle^{(1)} = \left(\overline{\sigma}_{eq}\right)^{n+1}\widetilde{U}_N(\boldsymbol{N}, X_\Sigma). \tag{5.2}$$

Due to the homogeneity of $\widetilde{U}$, it is noted that $\widetilde{U}_N(\boldsymbol{N}, X_\Sigma)$ is the same function in (5.1) and (5.2), and hence combination of these two equations gives

$$\overline{\Sigma}_{eq} = \left[(n+1)\dot{\gamma}_0^{-1}\tau_0^n\widetilde{U}(\overline{\boldsymbol{\sigma}})\right]^{\frac{1}{n+1}}\overline{\sigma}_{eq}. \tag{5.3}$$

In the FE code, $\overline{D}_{11}$ and the average X_Σ in the unit-cell are applied and remain constant throughout the process, as discussed in Section 4.2, whereby $\overline{D}_{22}$ and $\overline{\sigma}_{eq}$ are calculated. In addition, post-processing of the numerical results provides $\widetilde{U}(\overline{\boldsymbol{\sigma}})$ (via definition (2.2)). Finally, $\overline{\Sigma}_{eq}$ is readily obtained from Eq. (5.3), while $\overline{\Sigma}_m = X_\Sigma\overline{\Sigma}_{eq}$ given the known stress triaxiality X_Σ.

At this point it is perhaps necessary to clarify that the present work focuses on two-dimensions (i.e., plane-strain loadings) and the porous crystal exhibits two types of anisotropy. The first is that of the crystal matrix and the corresponding slip systems and the second is that of the void shape which is elliptical in general. Therefore, the effective response of the porous crystal is a function of all the three in-plane stress components $\overline{\sigma}_{11}$, $\overline{\sigma}_{22}$ and $\overline{\sigma}_{12}$ (or equivalently $\overline{\Sigma}_{11}$, $\overline{\Sigma}_{22}$ and $\overline{\Sigma}_{12}$). Following traditional notation in the context of porous materials, the following results are broken down into two major groups. The first group shows the effective response of the porous crystals in the space $\overline{\Sigma}_m - \overline{\Sigma}_{eq}$, which is equivalent to setting $\overline{\Sigma}_{12} = 0$ and working in the space $\overline{\sigma}_{11} - \overline{\sigma}_{22}$. This stress space is very important since it involves directly the hydrostatic component $\overline{\Sigma}_m$. The second group shows results in the deviatoric plane as this is defined by the in-plane shear stresses $(\overline{\Sigma}_{11} - \overline{\Sigma}_{22})/2 - \overline{\Sigma}_{12}$, and for given constant hydrostatic stress $\overline{\Sigma}_m$. This way, our results are complete in the sense that they cover the entire stress space but using traditional and well-understood stress measures, as discussed above.

5.2. Purely hydrostatic loadings for circular voids

In this section, we present results for the effective behavior of porous single crystals submitted to purely hydrostatic loadings for a range of creep exponents $n = (1, 2, 5, 10)$ and porosities $f = (1\%, 5\%)$.

First, we consider the case of K "equiangular" slip systems (i.e., systems forming equal angles with each other in the interval $[-\pi/2, \pi/2]$). Fig. 3 shows MVAR and FE comparisons for the average hydrostatic stress $\overline{\Sigma}_m$ as a function of the number of slip systems K. The MVAR is found to be in very good agreement with the FE results for the entire range of creep exponents (i.e., nonlinearities) n and porosities f considered here. Rather interestingly, for large values of $n = 5, 10$ a slightly non-monotonic response is observed in the FE calculations for $K = 4$ slip systems, as observed in Fig. 3(c) and (d), and in this specific case the MVAR model tends to underestimate slightly the value of the hydrostatic point for $K = 4$. Moreover, as K increases we attain the isotropic limit where the Composite Cylinder Assemblage (CCA) result in Eq. (3.23) has been used to correct the original VAR model.

Interestingly, it is found that for highly anisotropic equiangular crystals, $K = 1$ and $K = 2$ (with 90^o angle between the systems) the obtained hydrostatic point is infinite, i.e., the porous single crystal is incompressible, and thus it is not shown in Fig. 3. In order to further analyze this very critical effect, we consider next crystals with $K = 2$ slip systems that form arbitrary angles $\theta^{(1,2)}$. The porosity is set equal to $f = 1\%$ (the conclusions drawn in this case are independent of the porosity considered) and the creep exponents are $n = (1, 2, 5, 10)$. A parametric study of the relative angle

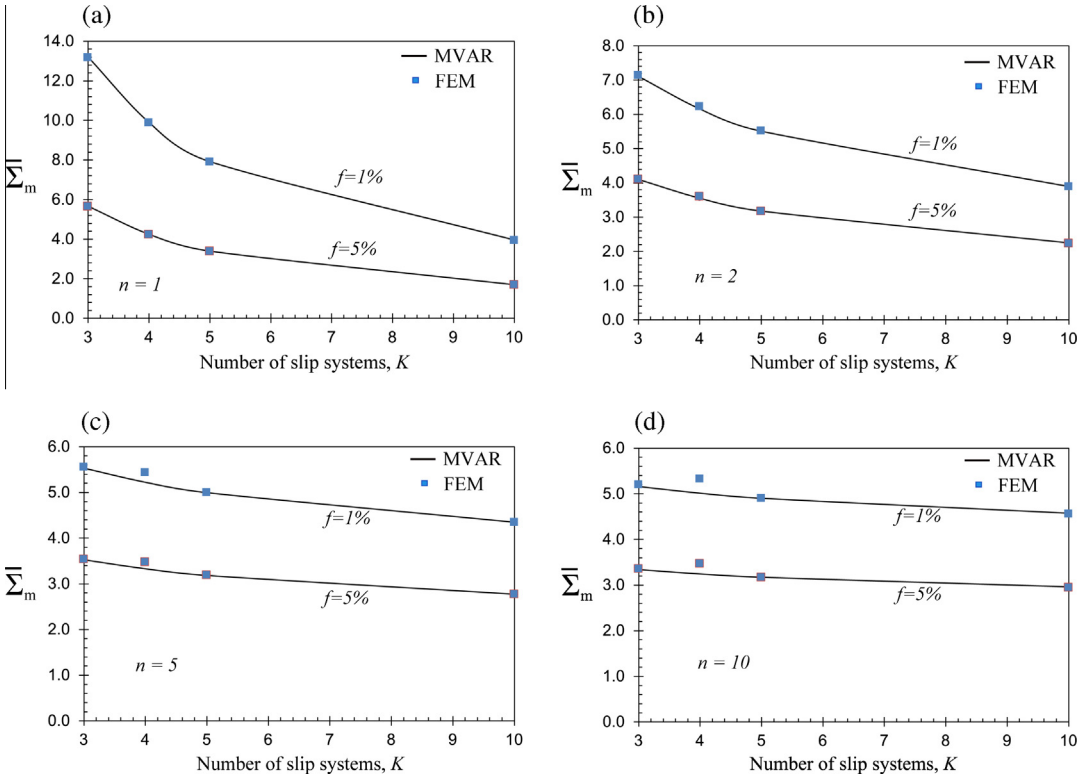

Fig. 3. Comparison between the average hydrostatic stress obtained by the model (MVAR) and the one resulting from FE results for a range of porosity $f = (1\%, 5\%)$, in the cases of $K = (3, 4, 5, 10)$ "equiangular slip systems" for (a) $n = 1$, (b) $n = 2$, (c) $n = 5$, (d) $n = 10$.

$\Delta\theta = \theta^{(1)} - \theta^{(2)} = (20^\circ, 30^\circ, 40^\circ, 45^\circ, 50^\circ, 60^\circ, 70^\circ)$ between the two slip systems is carried out next. It is mentioned however, that in the case of highly anisotropic crystals (i.e., $0^\circ < \Delta\theta < 20^\circ$ and $70^\circ < \Delta\theta < 90^\circ$) the numerical simulations exhibit convergence issues and thus no FE results are shown in this range (see also Willot et al., 2008). In this regard, Fig. 4 presents MVAR and FE normalized average hydrostatic stresses, $\overline{\Sigma}_m(\Delta\theta = 45^\circ)/\overline{\Sigma}_m$ as function of the difference between slip orientations $\Delta\theta$, for several creep exponents. The major observation in the context of this figure is that for $\Delta\theta = 0^\circ$ (i.e., $K = 1$ slip system) and $\Delta\theta = 90^\circ$ (i.e., equiangular slip systems) the normalized stresses $\overline{\Sigma}_m(\Delta\theta = 45^\circ)/\overline{\Sigma}_m = 0$ or equivalently $\overline{\Sigma}_m \to \infty$. This implies that even if pores are present in this case the effective porous crystal response is entirely *incompressible* for all creep exponents considered here. This result suggests that for such low symmetry crystals certain directions appear as "rigid" to plastic deformation thus constraining slip under highly symmetric loads such as purely hydrostatic tension or compression.

In turn, the maximum value of $\overline{\Sigma}_m(\Delta\theta = 45^\circ)/\overline{\Sigma}_m$ (i.e., the minimum value for $\overline{\Sigma}_m$) is found for $\Delta\theta = 45^\circ$. More specifically, as observed in Fig. 4(a) ($n = 1$) and Fig. 4(b) ($n = 2$), there is very good agreement between the MVAR and the FE for all slip orientations considered, as expected for small nonlinearities. The agreement becomes less good for higher creep exponents $n = 5, 10$ but still remains relatively good.

5.3. Gauge surfaces for circular voids

Fig. 5 shows cross-sections of the effective gauge surfaces in the $\overline{\Sigma}_m - \overline{\Sigma}_{eq}$ plane in the case of a single crystal comprising $K = 3$ slip

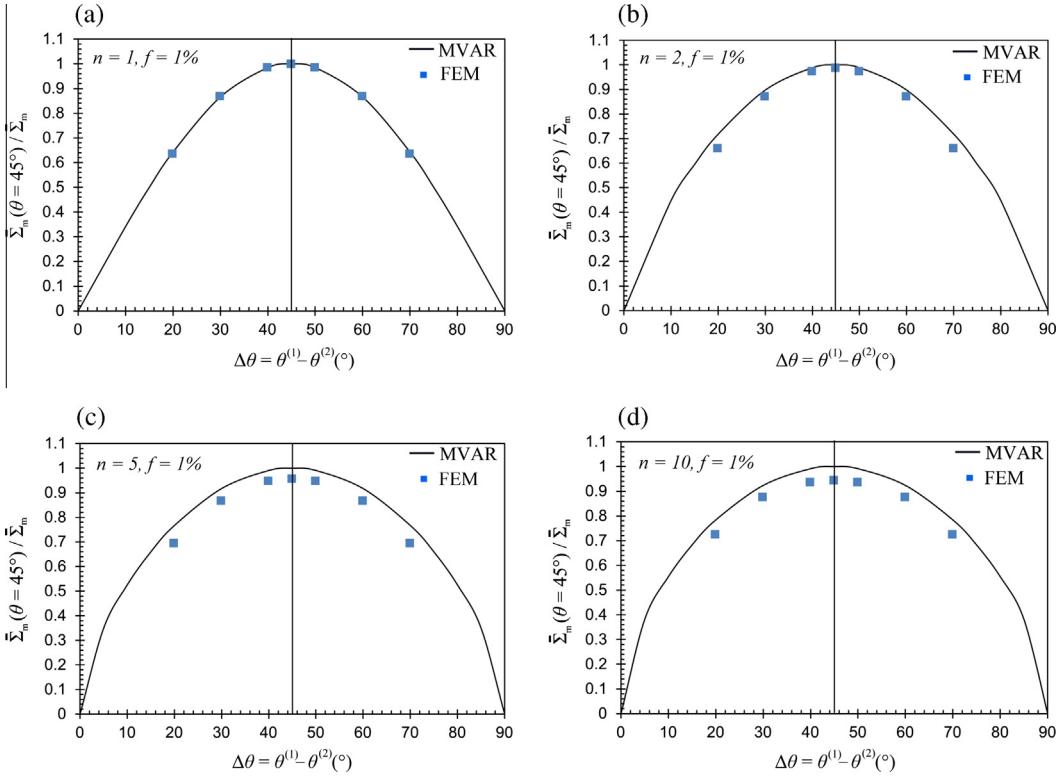

Fig. 4. Comparison between the average normalized hydrostatic stress obtained by the model (MVAR) and the one resulting from FE results for a single porous crystal $K = 2$ slip systems, a porosity $f = 1\%$ and a range of slip orientations $\Delta\theta = (20^\circ, 30^\circ, 40^\circ, 45^\circ, 50^\circ, 60^\circ, 70^\circ)$ in the cases (a) $n = 1$, (b) $n = 2$, (c) $n = 5$, (d) $n = 10$.

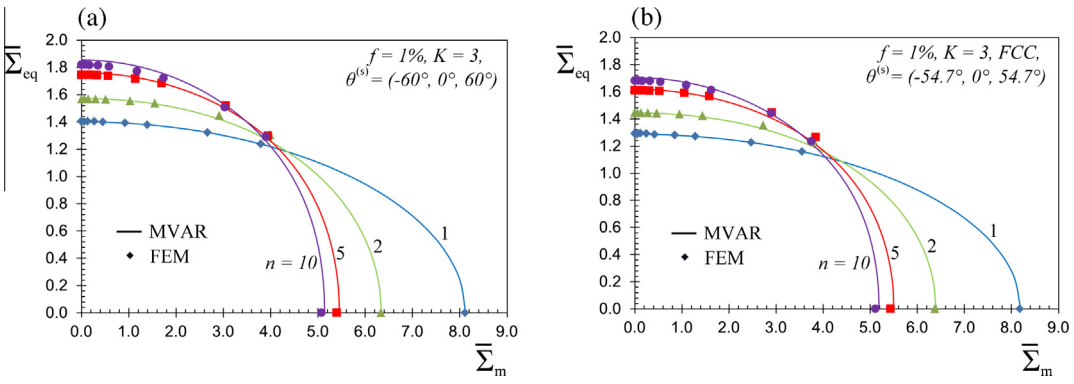

Fig. 5. Gauge surfaces in the $\overline{\Sigma}_m - \overline{\Sigma}_{eq}$ plane for a porous single crystal with circular voids of $K = 3$ slip systems, a porosity $f = 1\%$ and a range of creep exponent $n = (1, 2, 5, 10)$. Comparison between the model (MVAR) and the FE results in the cases of (a) slip orientations $\theta^{(s)} = (-60^\circ, 0^\circ, 60^\circ)$ (equiangular), (b) slip orientations $\theta^{(s)} = (-54.7^\circ, 0^\circ, 54.7^\circ)$ (FCC).

systems with slip orientations (a) $\theta^{(s)} = (-60^\circ, 0^\circ, 60^\circ)$ (equiangular slip systems) and (b) $\theta^{(s)} = (-54.7^\circ, 0^\circ, 54.7^\circ)$ which correspond to a face cubic-centered (FCC) single crystal in the 2-dimensional context (Rice, 1987). Various creep exponents $n = (1, 2, 5, 10)$ are considered while the porosity is set to $f = 1\%$. In the context of this figure, we observe a very good agreement between the MVAR predictions and the FE results for the entire range of creep exponents n. A rather interesting observation is that as the nonlinearity n increases the porous crystal becomes more compliant at large values of $\overline{\Sigma}_m$ (i.e., high triaxialities) but more stiff at small $\overline{\Sigma}_m$ (i.e. low stress triaxialities). As a consequence this leads to the inter-crossing of the curves corresponding to different n as observed in Fig. 5. Finally, it is perhaps useful to note that the important effect of the creep exponent n for zero triaxiality is merely an effect deriving from purely crystal plasticity even without the presence of voids.

In Fig. 6, we present cross-sections of the effective gauge surfaces in the $\overline{\Sigma}_m - \overline{\Sigma}_{eq}$ plane in the case of $K = 2$ slip systems crystal for a porosity $f = 1\%$ and the same range of creep exponents. Specifically we consider slip orientations (a) $\theta^{(s)} = (-22.5^\circ, 22.5^\circ)$ and (b) $\theta^{(s)} = (-15^\circ, 15^\circ)$. The main observation in the context of this figure is that for several slip orientations as well as for several number of slip systems (see previous cases with $K = 3$), there is a very good agreement between the MVAR predictions and the FE results for $f = 1\%$, at the full range of creep exponents and the entire range of the stress triaxialities considered here.

In order to assess the accuracy of the MVAR model at higher porosities $f = 5\%$ we carry out FE simulations using the more complex periodic unit-cell presented in Fig. 1(c). As detailed further in the next section, at $f = 5\%$ the void interactions become much more critical and thus a square unit-cell with one single void in the middle can lead to inconsistent comparisons when compared with the corresponding MVAR estimates for isotropic pore distributions (i.e., aspect ratio $w = 1$). In this regard, Fig. 7 shows cross-sections of the effective gauge surfaces in the $\overline{\Sigma}_m - \overline{\Sigma}_{eq}$ plane in the case of a higher porosity $f = 5\%$ and single crystals comprising (a) $K = 3$ slip systems with slip orientations $\theta^{(s)} = (-54.7^\circ, 0^\circ, 54.7^\circ)$ (FCC) and (b) $K = 2$ slip systems with slip orientations $\theta^{(s)} = (-15^\circ, 15^\circ)$, respectively. Again, the agreement between the MVAR predictions and the FE results is very good for small nonlinearities $n = 1, 2$, whereas it tends to overestimate the effective response at higher ones (i.e., $n = 5, 10$). In any case, the maximum error is found to be in the order of ~6%. It is also noted that the MVAR model deals extremely well with increasing anisotropy, i.e., as we go from $K = 3$ to $K = 2$ slip systems.

As we will see next, these differences between the MVAR and FE results with increasing nonlinearity (i.e., creep exponent) can be attributed to the increasing void interaction at high n.

5.4. Full field contours for periodic unit-cells

Following the last remark of the previous section, we show, next, contours of the total slip, defined as the sum of the absolute value of the slip on each individual slip system γ_{tot} normalized by the reference slip-rate $\dot{\gamma}_0$ (see Niordson and Kysar, 2014 for more details) for several periodic unit cells, porosities and creep exponents.

First, we consider the simplest periodic geometry which consists of a single pore in the middle of a square unit-cell such that

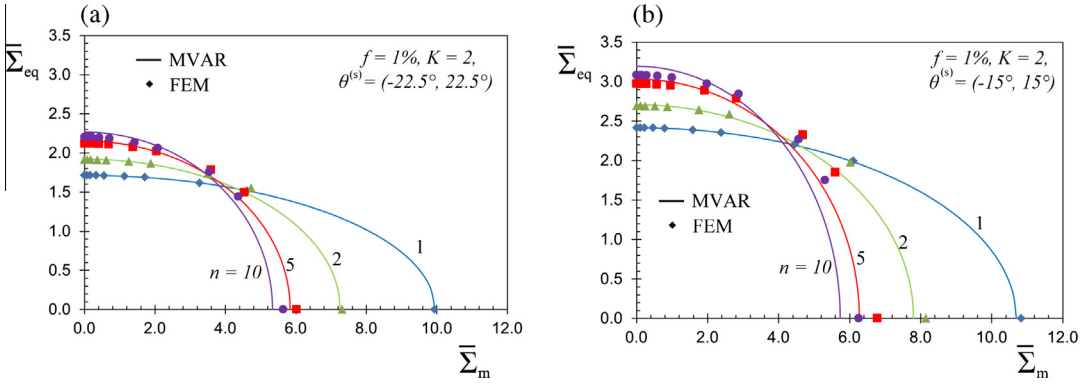

Fig. 6. Gauge surfaces in the $\overline{\Sigma}_m - \overline{\Sigma}_{eq}$ plane for a porous single crystal with circular voids of $K = 2$ slip systems, a porosity $f = 1\%$ and a range of creep exponent $n = (1, 2, 5, 10)$. Comparison between the model (MVAR) and the FE results in the cases of (a) slip orientations $\theta^{(s)} = (-22.5^\circ, 22.5^\circ)$, (b) slip orientations $\theta^{(s)} = (-15^\circ, 15^\circ)$.

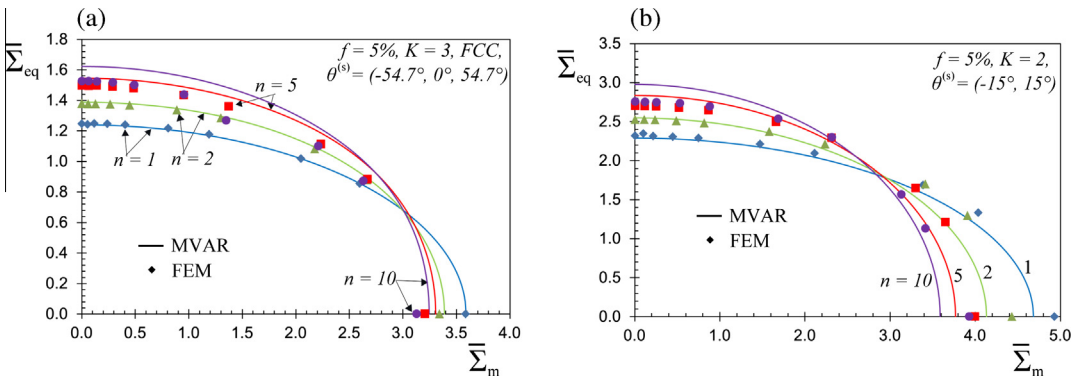

Fig. 7. Gauge surfaces in the $\overline{\Sigma}_m - \overline{\Sigma}_{eq}$ plane for a porous single crystal with circular voids of a porosity $f = 5\%$ and a range of creep exponent $n = (1, 2, 5, 10)$. Comparison between the model (MVAR) and the FE results in the cases of (a) $K = 3$ slip systems and slip orientations $\theta^{(s)} = (-54.7^\circ, 0^\circ, 54.7^\circ)$ (FCC), (b) $K = 2$ slip systems and slip orientations $\theta^{(s)} = (-15^\circ, 15^\circ)$.

the porosity $f = 1\%$. Fig. 8 shows countours of $\gamma_{tot}/\dot{\gamma}_0$ for $n = 10, K = 3$ equiangular slip systems and three applied stress triaxialities (a) $X_\Sigma = 0$, (b) $X_\Sigma = 3$ and (c) $X_\Sigma \to \infty$ (i.e., pure hydrostatic tension). A dramatic change of the deformation mechanism is observed as one goes from low X_Σ (see Fig. 8(a)) to high ones (see Fig. 8(c)). While for $X_\Sigma = 0$ the deformation map exhibits a 90° symmetry, as we increase hydrostatic tension the fields become highly localized around the pore geometry exhibiting 12-fold symmetry as already observed by Niordson and Kysar (2014) in this last case. At a value of $X_\Sigma = 3$ in Fig. 8(b), the slip fields show a combination of both of the above observed symmetries.

In the following, we analyze the results obtained for a unit-cell comprising a large number of isotropically distributed voids, as described in Section 4. More specifically, in Fig. 9, we consider purely hydrostatic loads (i.e., $X_\Sigma \to \infty$) with three different creep exponents $n = 1, 5, 10$ and two porosities $f = 1, 5\%$. First, we compare the effect of the porosity and subsequently the effect of the nonlinearity n upon the obtained fields. Comparison of Fig. 9(a)–(c) with the corresponding Fig. 9(d) and (e) shows that when $f = 1\%$ the total slip $\gamma_{tot}/\dot{\gamma}_0$ is rather concentrated around each individual pore even for larger exponents n. In contrast when $f = 5\%$, the pore interactions become more significant as expected. Moreover, in the case of $f = 5\%$, we observe a gradual deformation localization with increasing nonlinearity n as one goes from Fig. 9(d) and (e). The pore interaction and deformation localization becomes so pronounced that material around a significant number of pores is not at all loaded. This effect is much less pronounced when $f = 1\%$ and $n = 10$ in Fig. 9(c). These last observations imply

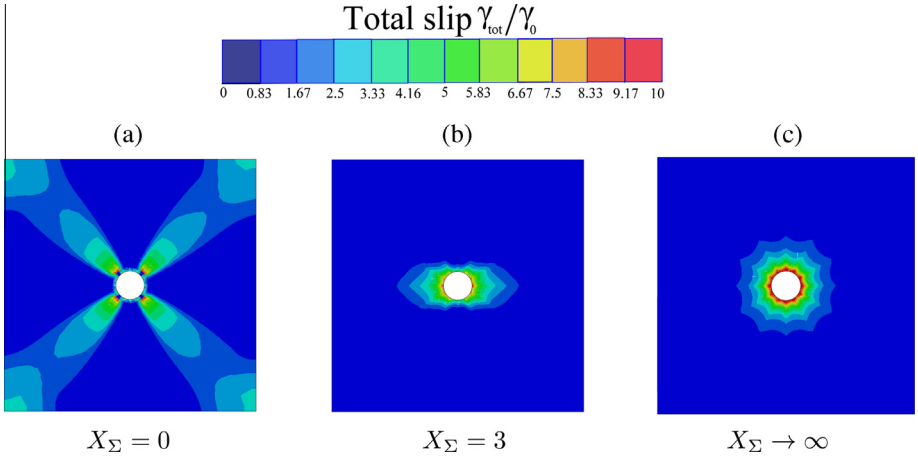

Fig. 8. Contour of the total slip for a $K = 3$ equiangular slip systems with a "one pore" geometry and a porosity of $f = 1\%$. Case of (a) $X_\Sigma = 0$ (b) $X_\Sigma = 3$ and (c) $X_\Sigma = \infty$.

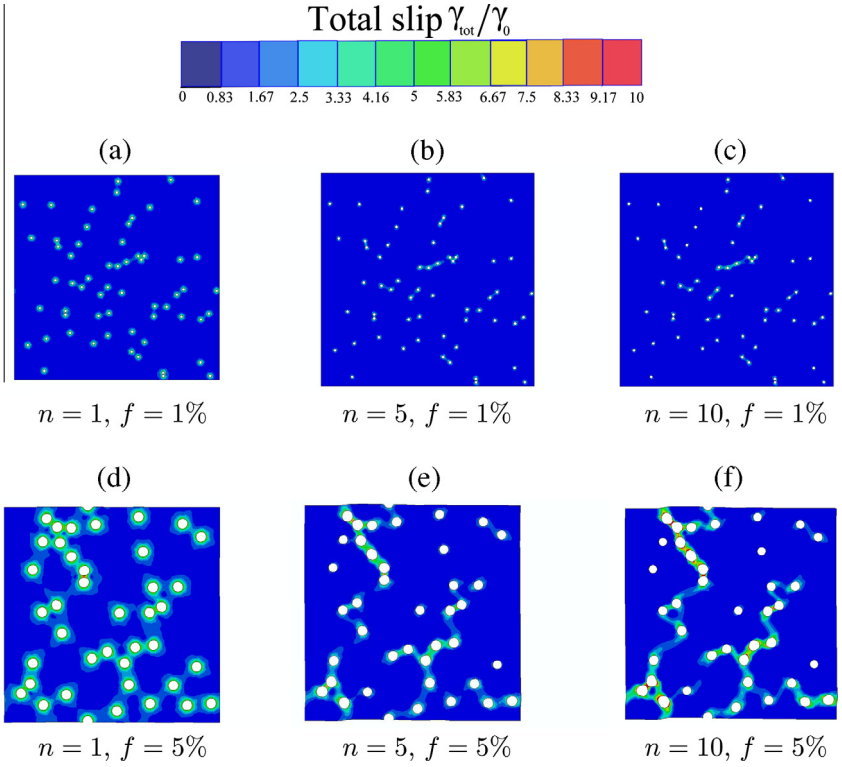

Fig. 9. Contour of the total slip for a FCC single crystal with two "multipore" geometries of 60 pores ($f = 1\%$) and 40 pores ($f = 5\%$), in macroscopic hydrostatic loading state ($X_\Sigma = \infty$). Case of (a) $f = 1\%,\ n = 1$ (b) $f = 1\%,\ n = 5$ (c) $f = 1\%,\ n = 10$ (d) $f = 5\%,\ n = 1$ (e) $f = 5\%,\ n = 5$ (f) $f = 5\%,\ n = 10$.

that for low porosities $f = 1\%$ the use of the simpler unit-cell shown in Fig. 8 is accurate enough, while for larger porosities (even for 5%) the pore interactions become non-negligible and unit-cells with large number of pores should be used. Finally, this strong deformation localization observed in Fig. 8(e) explains why the MVAR model is in less good agreement with the FE with increasing creep exponent n and increasing porosity f.

5.5. Macroscopic strain-rates for circular voids

In this section, for the sake of conciseness, we present only representative results for the macroscopic strain-rates. Those constitute a direct measure of the normal (i.e., slope) to the previously shown gauge surfaces and hence have important implications on the developed plastic anisotropy as well as void growth (see Danas et al., 2008). More specifically, Fig. 10 shows the average strain-rates in the $\overline{D}_m - \overline{D}_{eq}$ plane in the case of a single crystal comprising (a) $K = 3$ slip systems with slip orientations $\theta^{(s)} = (-54.7^\circ, 0^\circ, 54.7^\circ)$ (FCC) and (b) $K = 2$ slip systems with slip orientations $\theta^{(s)} = (-22.5^\circ, 22.5^\circ)$. Results are obtained for several creep exponents $n = (1, 2, 5, 10)$ and a porosity $f = 1\%$. As observed in the context of this figure, the MVAR predictions are in good agreement with the FE results for the entire range of parameters used. Conversely with the corresponding gauge surfaces, the hydrostatic strain-rate $\overline{D}_m$ increases with increasing n at high triaxialities and vice verse for low triaxialities. This has direct implications on the corresponding void growth at large triaxialities and as already expected (Danas and Ponte Castañeda, 2009b) the voids will grow much faster at higher creep exponents n and higher triaxialities.

5.6. Gauge surfaces for elliptical voids

In this subsection, we show results for porous single crystals comprising elliptical voids, i.e., with aspect ratio $w \neq 1$ and angles $\psi \neq 0$. The first microstructure considered is defined by porosity $f = 1\%$, void aspect ratio $w = 1/3$ and void orientation $\psi = 0$. Fig. 11 presents various cross-sections of the effective gauge surfaces in the $\overline{\Sigma}_m - \overline{\Sigma}_{eq}$ plane in the case of $K = 3$ slip systems with slip orientations $\theta^{(s)} = (-60^\circ, 0^\circ, 60^\circ)$ (equiangular slip systems) and creep exponents $n = (1, 10)$. In the context of this figure, the MVAR predictions are in relatively good agreement with the FE results for both $n = (1, 10)$. In particular, for $n = 1$, the MVAR is in excellent agreement with the FE results except at purely hydrostatic loadings where an error in the order of 7% is observed. Nonetheless, in that case numerical convergence issues appeared

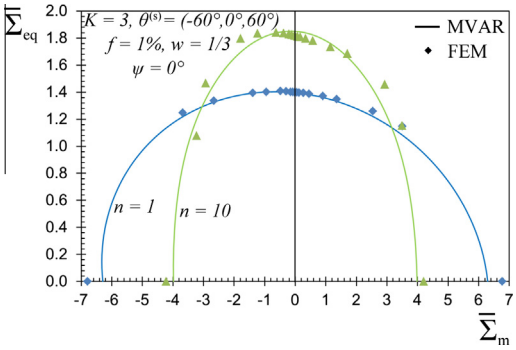

Fig. 11. Gauge surfaces in the $\overline{\Sigma}_m - \overline{\Sigma}_{eq}$ plane for a single porous crystal with elliptical voids ($w = 1/3$, $\psi = 0^\circ$) of $K = 3$ slip systems, $f = 1\%$, slip orientations $\theta^{(s)} = (-60^\circ, 0^\circ, 60^\circ)$ (equiangular) and a range of creep exponent $n = (1, 10)$. Comparison between the MVAR model and the FE results.

and the FE results should be interpreted with caution. In turn, when $n = 10$, the MVAR exhibits very good qualitative agreement with the FE results where the corresponding gauge surface exhibits a rather significant "asymmetry" with respect to the $\overline{\Sigma}_{eq}$ axis but tends to underestimate this effect especially at small stress triaxialities (i.e., for $\overline{\Sigma}_m \sim 0$). This asymmetry, which is present in the case of elliptical voids, is a direct consequence of the coupling between $\overline{\Sigma}_m$ and $\overline{\Sigma}_{eq}$ resulting from the complex form of the tensor $\mathbf{G}$ defined in Eq. (3.14). Such effects observed in shearing of ellipsoidal voids have also been addressed either in numerical micromechanical calculations (see for instance Tvergaard and Nielsen, 2010), or in multiaxial experiments (see Combaz et al., 2011).

To summarize, the MVAR model has been assessed in great detail and it was found to be in good agreement with the corresponding FE results. Therefore, for simplicity and conciseness, only MVAR estimates will be shown in the following section.

6. Results: MVAR predictions

Hereafter, we attempt to reveal the complex coupling between the crystal anisotropy as characterized by the number of slip systems and their orientation, and the (morphological) void anisotropy resulting from the elliptical void shape and orientation.

6.1. Effect of the void shape and orientation

More specifically, Fig. 12 shows MVAR gauge surfaces in the $\overline{\Sigma}_m - \overline{\Sigma}_{eq}$ plane for a porous single crystal comprising $K = 3$ slip

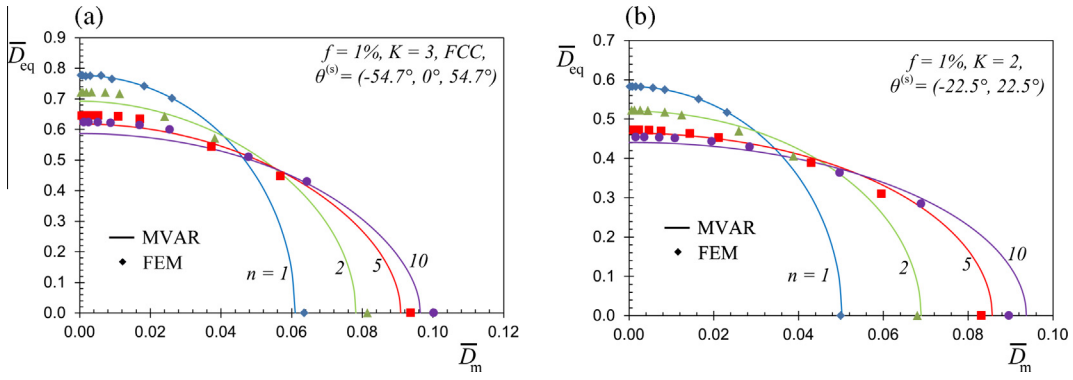

Fig. 10. Macroscopic strain-rates in the $\overline{D}_m - \overline{D}_{eq}$ plane for a porous single crystal with circular voids of a porosity $f = 1\%$ and a range of creep exponent $n = (1, 2, 5, 10)$. Comparison between the model (MVAR) and the FE results in the cases of (a) $K = 3$ slip systems and slip orientations $\theta^{(s)} = (-54.7^\circ, 0^\circ, 54.7^\circ)$ (FCC) and (b) $K = 2$ slip systems and slip orientations $\theta^{(s)} = (-22.5^\circ, 22.5^\circ)$.

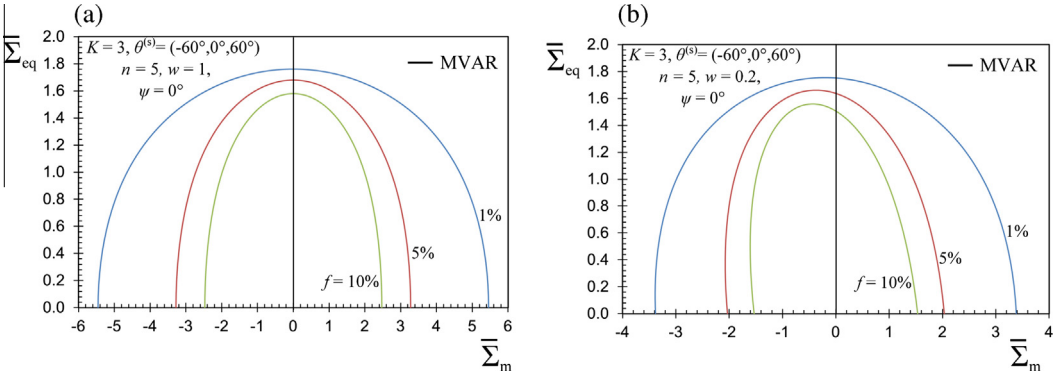

Fig. 12. Gauge surfaces in the $\overline{\Sigma}_m - \overline{\Sigma}_{eq}$ plane for a single porous crystal with elliptical voids, $K = 3$ slip systems with slip orientations $\theta^{(s)} = (-60^\circ, 0^\circ, 60^\circ)$ and a creep exponent $n = 5$. The effect of porosity is investigated by choosing $f = (1\%, 5\%, 10\%)$ for different void shapes (a) $w = 1,\ \psi = 0^\circ$ and (b) $w = 0.2,\ \psi = 0^\circ$.

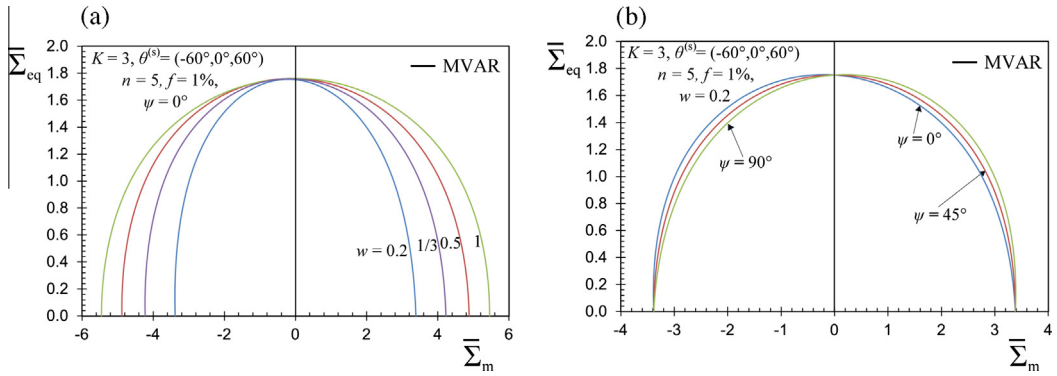

Fig. 13. Gauge surfaces in the $\overline{\Sigma}_m - \overline{\Sigma}_{eq}$ plane for a single porous crystal with elliptical voids, $K = 3$ slip systems, slip orientations $\theta^{(s)} = (-60^\circ, 0^\circ, 60^\circ)$ and a creep exponent $n = 5$. The porosity of set to $f = 1\%$. The effect of (a) the void aspect ratio is investigated by choosing $w = (0.2, 0.5, 1)$ for an angle $\psi = 0$ and (b) of the void orientation by choosing $\psi = (0^\circ, 45^\circ, 90^\circ)$ for a given aspect ratio $w = 0.2$.

systems with slip orientations $\theta^{(s)} = (-60^\circ, 0^\circ, 60^\circ)$ (i.e., equiangular slip systems) and a creep exponent $n = 5$. The effect of porosity is investigated by choosing $f = (1\%, 5\%, 10\%)$ for different void shapes (a) $w = 1,\ \psi = 0^\circ$ and (b) $w = 0.2,\ \psi = 0^\circ$. In Fig. 12, the gauge surfaces exhibit a gradual decrease with increasing porosity for both circular ($w = 1$) and elliptic ($w = 0.2$) voids, as already expected. Nonetheless, while for the case of a circular void ($w = 1$), in Fig. 12(a), the curves are symmetric with respect to the $\overline{\Sigma}_{eq}$ axis, the curves for the elliptical void ($w = 0.2$), in Fig. 12(b), become asymmetric as already discussed in the context of Fig. 11. As a consequence of this asymmetry, the MVAR estimates are found to be stiffer in the negative pressure regime ($\overline{\Sigma}_m < 0$). The observed asymmetry becomes more pronounced with increasing porosity.

Fig. 13 shows gauge surfaces in the $\overline{\Sigma}_m - \overline{\Sigma}_{eq}$ plane for a single porous crystal comprising $K = 3$ slip systems with slip orientations $\theta^{(s)} = (-60^\circ, 0^\circ, 60^\circ)$ and a creep exponent $n = 5$. The porosity of set to $f = 1\%$. The effect of (a) the void aspect ratio is investigated by choosing $w = (0.2, 0.5, 1)$ for an angle $\psi = 0$ and (b) of the void orientation by choosing $\psi = (0^\circ, 45^\circ, 90^\circ)$ for a given aspect ratio $w = 0.2$. In Fig. 13(a), we observe that with decreasing w, the gauge surface becomes gradually asymmetric while diminishing in size. This last effect implies that for the same porosity $f = 1\%$, an elliptical void $w < 1$ leads to softer response than a circular one.

In Fig. 13(b), we study the effect of the void orientation angle $\psi = (0^\circ, 45^\circ, 90^\circ)$. Note that the case $\psi = 90^\circ$ is equivalent to setting $w \to 1/w$ and $\psi = 0^\circ$. In particular, the $\psi = 90^\circ$ curve is simply a reflection of that for $\psi = 0^\circ$ about the $\overline{\Sigma}_{eq}$ axis, as naturally expected from purely geometrical arguments. In turn, the $\psi = 45^\circ$ curve exhibits full symmetry with respect to the $\overline{\Sigma}_{eq}$ axis contrary to the other two cases $\psi = 0^\circ, 90^\circ$. Finally, as already expected from earlier studies (Danas and Ponte Castañeda, 2009b), the hydrostatic point for all these cases is independent of the angle ψ. This is intuitively expected since the hydrostatic loading has no preferential direction and can be easily attributed to the form of the $\mathbf{G}$ tensor defined in Eq. (3.14), since the sum of its diagonal components $\mathbf{G}_{1111} + 2\mathbf{G}_{1122} + \mathbf{G}_{2222} = w^2 + 1$, is independent of the angle ψ.

6.2. Effect of the crystal anisotropy

In this subsection, we discuss in more detail the effect of matrix crystal anisotropy upon the effective response of the porous composite. As already discussed in the context of Fig. 4, where circular voids are embedded in a two slip systems single crystal, the average hydrostatic response is strongly influenced by the slip orientations. Specifically, both the MVAR model and the FE results predict that the effective behavior of a porous single crystal with $K = 1$ slip system (i.e., highly anisotropic case) or $K = 2$ slip systems with 90° relative angle lead to a completely incompressible response.

In order to analyze this further, Fig. 14 shows gauge surfaces in the $\overline{\Sigma}_m - \overline{\Sigma}_{eq}$ plane of porous single crystals with circular voids ($w = 1$), porosity $f = 5\%$ and a creep exponent $n = 10$. In order to reveal the effect of the number of slip systems as well as of their orientations upon the effective response of the porous crystal, we consider the case of $K = (1, 2, 3, 4, 5)$ with (a) equiangular slip system orientations and (b) with arbitrary non-equiangular slip

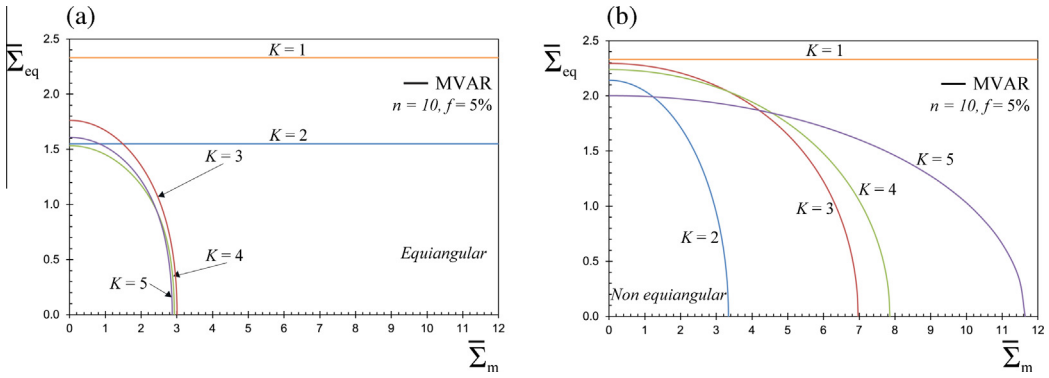

Fig. 14. Gauge surfaces in the $\overline{\Sigma}_m - \overline{\Sigma}_{eq}$ plane for a single porous crystal with circular voids, porosity $f = 5\%$, creep exponent $n = 10$, for several number of slip systems $K = (1, 2, 3, 4, 5)$. Part (a) corresponds to equiangular and (b) to non-equiangular slip system orientations. Their precise definition is detailed in Table 2.

system orientations. The specific choices of the different orientations can be found in Table 2 for both cases considered here.

6.2.1. Equiangular slip systems

More specifically, in Fig. 14(a), we observe a strong dependence of the effective response upon K. While for $K = 1$ and $K = 2$ the porous crystal exhibits a fully incompressible response (in agreement with the observations made in Fig. 4), the porous crystal becomes gradually softer with increasing K. On the other hand, one could observe that the response for $K = 3, 4, 5$ is very similar quantitatively, especially near the hydrostatic point (i.e., $\overline{\Sigma}_{eq} = 0$).

6.2.2. Non equiangular slip systems

By contrast, in Fig. 14(b), we observe an even stronger dependence of the effective response upon the crystal anisotropy. In this case, the porous crystal is still incompressible for $K = 1$ but not for the rest of the cases $K \geqslant 2$. In addition, in Fig. 14(b), the dependence of the effective response for $K \geqslant 2$ at moderate and high triaxialities is completely reversed (for instance, the material with $K = 2$ is softer than those for $K = 3$ or $K = 4$) when compared to that in Fig. 14(a).

At this point, it is perhaps relevant to make contact with the corresponding three-dimensional models proposed by Han et al. (2013) and Paux et al. (2015). In these models—which have been assessed for an FCC crystal (near equiangular case in our notation)—even though the deviatoric response includes the effect of the crystal anisotropy (i.e., number of slip systems and orientations), the corresponding response under purely hydrostatic stressing is, at least in its present form, independent of the orientation of the slip systems. The present study, albeit in two-dimensions, shows that in the context of highly anisotropic porous single crystals, the purely hydrostatic response is extremely sensitive to the number of the slip systems K as well as on the slip orientations, as clearly shown in Fig. 14. Of course, the present model needs to be extended in the three-dimensional case in order to have a more complete picture of the coupling between crystal anisotropy and (morphological) void anisotropy. Such work is underway and therein comparisons will be given with available models in the literature.

6.3. Fully anisotropic effective response on the deviatoric plane

In this section, we investigate the effective response of the porous single crystal in the deviatoric plane $\overline{\Sigma}_{12} - (\overline{\Sigma}_{11} - \overline{\Sigma}_{22})/2$ for given hydrostatic stress $\overline{\Sigma}_m$. This allows to probe the complete response of the porous crystal and reveal in a more clear way the combined coupling between the anisotropy of crystal and that induced by the void shape and orientation. For the sake of conciseness, in the following, we consider only crystals comprising $K = 3$ slip systems with slip orientations $\theta^{(s)} = (-54.7°, 0°, 54.7°)$ (FCC) and $K = 2$ slip systems with slip orientations $\theta^{(s)} = (-22.5°, 22.5°)$, respectively, porosity $f = 5\%$ and creep exponent $n = 10$.

First, for illustration purposes and in order to give the reader a more complete viewpoint of the porous crystal effective response, we show in Fig. 15 two representative three-dimensional gauge surfaces defined by the axes $\overline{\Sigma}_{12} - (\overline{\Sigma}_{11} - \overline{\Sigma}_{22})/2 - \overline{\Sigma}_m$ for (a) $K = 3$ and (b) $K = 2$. The void aspect ratio and orientation are set to $w = 0.2$ and $\psi = 0$, respectively. Further discussion of these (and even more) surfaces is done in the following by considering projections in the deviatoric planes.

In this connection, Fig. 16 shows MVAR gauge surfaces in the deviatoric plane $\overline{\Sigma}_{12} - (\overline{\Sigma}_{11} - \overline{\Sigma}_{22})/2$ for a single porous crystal with $K = 3$ slip systems, slip orientations $\theta^{(s)} = (-54.7°, 0°, 54.7°)$, void shapes $w = (0.2, 1)$ and void orientations $\psi = (0°, 22.5°, 67.5°)$. The various cross-sections correspond to different hydrostatic stresses $\overline{\Sigma}_m = 0$, $\overline{\Sigma}_m = \pm 0.5\overline{\Sigma}_m^H$, $\overline{\Sigma}_m = \pm 0.9\overline{\Sigma}_m^H$, where $\overline{\Sigma}_m^H$ denotes the hydrostatic point delivered by the model MVAR for hydrostatic loading for each of the given cases in Fig. 16(a)–(d), respectively.

More specifically, in Fig. 16(a), which corresponds to a circular void, we observe a gradual shrinking of the curves with increasing $\overline{\Sigma}_m$ as expected. At small values of $\overline{\Sigma}_m = 0$, the curve exhibits an almost discrete character which tends to become more rounded (convexify) with increasing $\overline{\Sigma}_m$. Note at this point that since the porous crystal is considered to be rate-dependent (i.e., finite value of the creep exponent n), the corresponding effective response is strictly convex and the curves exhibit large but finite curvature areas (i.e., smooth-corners) leading to an almost hexagonal

Table 2
Set of angles $\theta^{(s)}$ for equiangular and non equiangular slip systems.

Type	$K = 1$	$K = 2$	$K = 3$	$K = 4$	$K = 5$
Equiangular	$\theta^{(s)} = \pi/8$	$\theta^{(s)} = \{\pm\pi/4\}$	$\theta^{(s)} = \{0, \pm\pi/3\}$	$\theta^{(s)} = \{0, \pm\pi/4, \pi/2\}$	$\theta^{(s)} = \{0, \pm\pi/5, \pm 2\pi/5\}$
Non equiangular	$\theta^{(s)} = \pi/8$	$\theta^{(s)} = \{\pm\pi/8\}$	$\theta^{(s)} = \{\pi/8, \pi/10, \pi/12\}$	$\theta^{(s)} = \{\pi/8, \pi/9, \pi/10, \pi/11\}$	$\theta^{(s)} = \{\pi/8, 2\pi/15, 4\pi/31, 4\pi/33, 2\pi/17\}$

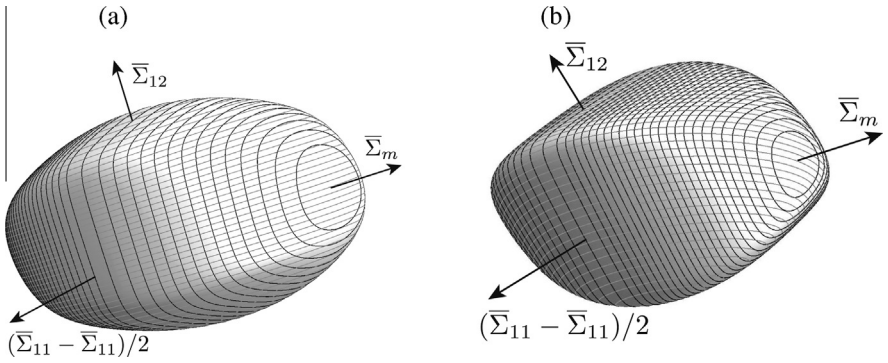

Fig. 15. Three-dimensional gauge surfaces defined by the axes $\overline{\Sigma}_{12} - (\overline{\Sigma}_{11} - \overline{\Sigma}_{22})/2 - \overline{\Sigma}_m$ for (a) $K = 3$ ($\theta^{(s)} = (-54.7^\circ, 0^\circ, 54.7^\circ)$) and (b) $K = 2$ ($\theta^{(s)} = (-22.5^\circ, 22.5^\circ)$). The void aspect ratio and orientation are set to $w = 0.2$ and $\psi = 0$, porosity is $f = 5\%$ and creep exponent $n = 10$.

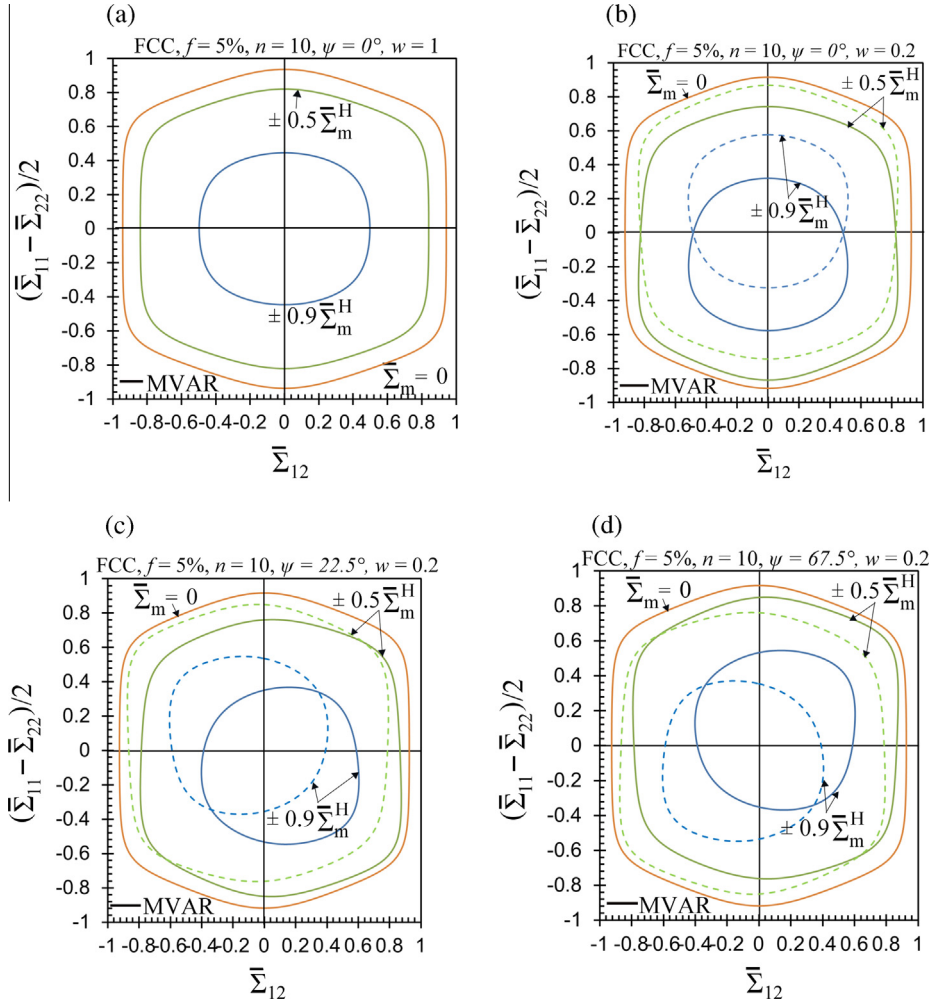

Fig. 16. Gauge surfaces in the deviatoric plane $\overline{\Sigma}_{12} - (\overline{\Sigma}_{11} - \overline{\Sigma}_{22})/2$ for a single porous crystal with elliptical voids, $K = 3$ slip systems, slip orientations $\theta^{(s)} = (-54.7^\circ, 0^\circ, 54.7^\circ)$ (FCC), a porosity $f = 5\%$, a creep exponent $n = 10$, at different level of pressure. The dashed line curves correspond to the negative pressure regime while the continuous one correspond to the positive pressure regime. Case of (a) $\psi = 0^\circ$, $w = 1$, (b) $\psi = 0^\circ$, $w = 0.2$, (c) $\psi = 22.5^\circ$, $w = 0.2$, (d) $\psi = 67.5^\circ$, $w = 0.2$.

symmetry of the curves. When the void is circular ($w = 1$), the porous crystal preserves the original symmetries of the crystal matrix for all values of $\overline{\Sigma}_m$ considered. In particular, in this case the curve is fully symmetric with respect to the two axes $\overline{\Sigma}_{12}$ and $(\overline{\Sigma}_{11} - \overline{\Sigma}_{22})/2$.

By contrast, as shown in Fig. 16(b) (see Fig. 15(a) for the three-dimensional surface), if one considers an elliptical void with aspect ratio $w = 0.2$ (but still $\psi = 0^\circ$), the corresponding MVAR curves exhibit an asymmetry with respect to the $\overline{\Sigma}_{12}$-axis, but still preserve the symmetry with respect to the $(\overline{\Sigma}_{11} - \overline{\Sigma}_{22})/2$ axis for $\overline{\Sigma}_m > 0$. Rather interestingly, the almost hexagonal symmetry still prevails for $\overline{\Sigma}_m = 0$. This response is a direct consequence of the geometric coupling of the crystal slip orientations and the void shape at finite hydrostatic stresses. Note further that point symmetry of the curves

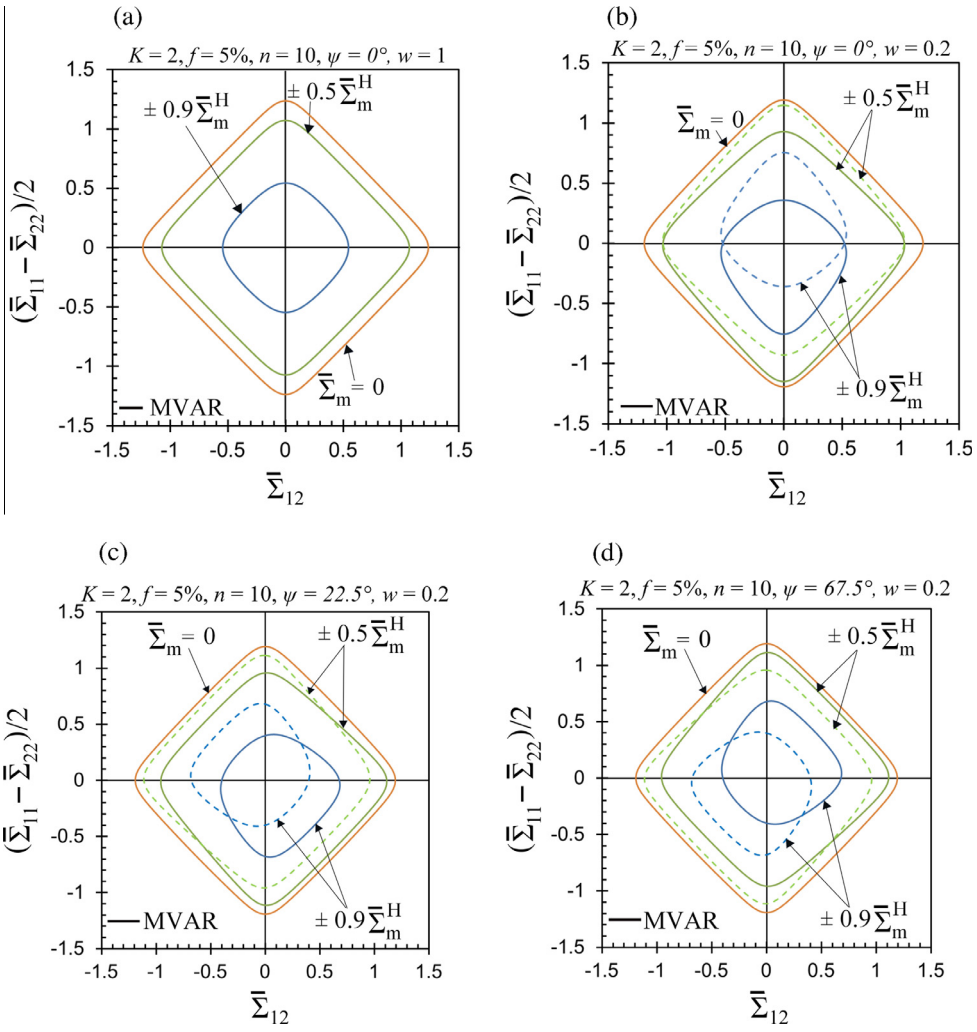

Fig. 17. Gauge surfaces in the deviatoric plane $\overline{\Sigma}_{12} - (\overline{\Sigma}_{11} - \overline{\Sigma}_{22})/2$ for a single porous crystal with elliptical voids, $K = 2$ slip systems, slip orientations $\theta^{(s)} = (-22.5°, 22.5°)$, a porosity $f = 5\%$, a creep exponent $n = 10$, at different level of pressure. The dashed line curves correspond to the negative pressure regime while the continuous one correspond to the positive pressure regime. Case of (a) $\psi = 0°$, $w = 1$, (b) $\psi = 0°$, $w = 0.2$, (c) $\psi = 22.5°$, $w = 0.2$, (d) $\psi = 67.5°$, $w = 0.2$.

with respect to the global origin $(\overline{\Sigma}_{12}, \pm(\overline{\Sigma}_{11} - \overline{\Sigma}_{22})/2) = (0,0)$ and $\overline{\Sigma}_m = 0$ is still preserved. This is easily observed by noting the point symmetries between the continuous lines corresponding to $\overline{\Sigma}_m > 0$ and the dashed ones for $\overline{\Sigma}_m < 0$.

Subsequently, in Fig. 16(c) and (d), an elliptical void ($w = 0.2$) with angles $\psi = 22.5°, 67.5°$ are shown, respectively. In these two cases, the gauge surfaces exhibit full asymmetry with respect to both axes for finite hydrostatic stresses $\overline{\Sigma}_m \neq 0$, but preserve the hexagonal symmetry for $\overline{\Sigma}_m = 0$. The observed asymmetry is much more pronounced at higher values of $\overline{\Sigma}_m$. Note that the curves for $\psi = 67.5$ in Fig. 16(d) can be reproduced from the $\psi = 22.5°$ ones in Fig. 16(c) by counter-clockwise rotation of 90° about the deviatoric origin $(\overline{\Sigma}_{12}, \pm(\overline{\Sigma}_{11} - \overline{\Sigma}_{22})/2) = (0,0)$. Again, it is stressed that point symmetry of the curves with respect to the global origin $(\overline{\Sigma}_{12}, \pm(\overline{\Sigma}_{11} - \overline{\Sigma}_{22})/2) = (0,0)$ and $\overline{\Sigma}_m = 0$ is still preserved if one compares the continuous ($\overline{\Sigma}_m > 0$) with the dashed lines ($\overline{\Sigma}_m < 0$).

Fig. 17 shows MVAR gauge surfaces in the deviatoric plane $\overline{\Sigma}_{12} - (\overline{\Sigma}_{11} - \overline{\Sigma}_{22})/2$ for a porous crystal with $K = 2$ slip systems, slip orientations $\theta^{(s)} = (-22.5^o, 22.5^o)$, void shapes $w = (0.2, 1)$ and void orientations $\psi = (0°, 22.5°, 67.5°)$. The various cross-sections correspond to different hydrostatic stresses $\overline{\Sigma}_m = 0, \overline{\Sigma}_m = \pm 0.5\overline{\Sigma}^H_m$ and $\overline{\Sigma}_m = \pm 0.9\overline{\Sigma}^H_m$, where $\overline{\Sigma}^H_m$ denotes the hydrostatic point delivered by the model MVAR for hydrostatic loading for each of the given cases in Fig. 17(a)–(d), respectively.

As observed in Fig. 17(a), which deals with circular voids, a gradual shrinking of the curves appears while increasing $\overline{\Sigma}_m$, as expected. Moreover, as also seen in the previous case, the curve exhibits an almost discrete character at small values of $\overline{\Sigma}_m = 0$ with tetragonal symmetry. These symmetries are preserved with the addition of hydrostatic stress even though some additional rounding is observed at high $\overline{\Sigma}_m = \pm 0.9\overline{\Sigma}^H_m$.

However, as shown in Fig. 17(b) (see Fig. 15(b) for the three-dimensional surface), for an elliptical void with aspect ratio $w = 0.2$ (but still $\psi = 0°$), the corresponding MVAR curves exhibit an asymmetry with respect to the $\overline{\Sigma}_{12}$ axis, but still preserve the symmetry with respect to the $(\overline{\Sigma}_{11} - \overline{\Sigma}_{22})/2$ axis for $\overline{\Sigma}_m > 0$. In addition, the almost tetragonal symmetry still prevails for $\overline{\Sigma}_m = 0$. As already discussed, this response is a direct consequence of the geometric coupling of the crystal slip orientations and the void shape at finite hydrostatic stresses. Note further that point symmetry of the curves with respect to the global origin $(\overline{\Sigma}_{12}, \pm(\overline{\Sigma}_{11} - \overline{\Sigma}_{22})/2) = (0,0)$ and $\overline{\Sigma}_m = 0$ is still preserved. Finally, in Fig. 17(c) and (d), an elliptical void ($w = 0.2$) with angles $\psi = 22.5°, 67.5°$ are shown, respectively. In these two cases, the gauge surfaces exhibit full asymmetry with respect to both axes

for finite hydrostatic stresses $\overline{\Sigma}_m \neq 0$, but preserve the tetragonal symmetry for $\overline{\Sigma}_m = 0$. As in the case of $K = 3$ slip systems, the curves for $\psi = 67.5$ in Fig. 17(d) can be reproduced from the $\psi = 22.5^\circ$ ones in Fig. 17(c) by counter-clockwise rotation of 90° about the deviatoric origin $(\overline{\Sigma}_{12}, \pm(\overline{\Sigma}_{11} - \overline{\Sigma}_{22})/2) = (0,0)$. Again, it is stressed that point symmetry of the curves with respect to the global origin $(\overline{\Sigma}_{12}, \pm(\overline{\Sigma}_{11} - \overline{\Sigma}_{22})/2) = (0,0)$ and $\overline{\Sigma}_m = 0$ is still preserved if one compares the continuous $(\overline{\Sigma}_m > 0)$ with the dashed lines $(\overline{\Sigma}_m < 0)$.

7. Conclusion

In this work, a fully analytical constitutive model has been developed for porous rate-dependent single crystals comprising cylindrical voids with elliptical cross-section, subjected to plane-strain loading conditions, accounting for full crystal anisotropy. In order to achieve this goal, the variational nonlinear homogenization method of Ponte Castañeda (1991a) has been used and modified (Danas and Aravas, 2012) to derive estimates but not bounds. The modified variational (MVAR) model presented in this study has been validated by comparison with full field FE calculations of single- and multi-void periodic unit-cells. The MVAR model has been found to be in good agreement with the FE results for a very wide range of parameters describing the number and orientation of the slip systems (i.e., crystal anisotropy), the creep exponent (i.e., nonlinearity) of the matrix crystal, the porosity and the void shapes and orientations. The MVAR model has shown strong predictive capabilities while exhibiting critical qualitative features.

Specifically, the MVAR model has been able to predict the strong dependence of the effective response, and especially of the average hydrostatic stress upon the number and orientation of the slip systems as well as the shape and orientation of the voids. The major finding of this work, is that for highly anisotropic crystals (e.g., one or even two active slip systems) the porous crystal can exhibit fully incompressible response, even in the presence of voids. This of course affects the entire effective response of the porous crystal for the entire range of stress states. That is the first time such a result is presented in the literature and reveals the significance of plastic anisotropy of the underlying phases upon the macroscopic response of the material. Furthermore, it has been shown that the void shape and orientation affect strongly the response of the porous crystal. In particular, the effective response becomes much softer as one goes from a circular void to an elliptical one (which is suggestive of a crack-type geometry). In the general case of elliptical voids oriented at an arbitrary angle (with respect to the laboratory axes) and arbitrary number of slip systems, we have shown that the effective response exhibits no symmetries when plotted in the purely deviatoric plane (and at finite hydrostatic stresses) thus indicating the non-trivial coupling between the anisotropy of the underlying crystal and the (morphological) anisotropy induced by the shape and orientation of the voids.

To the best knowledge of the authors, this is the first model—albeit in two-dimensions—in the literature that is able to deal with general crystal anisotropy, general void shapes and orientations and general in-plane loading conditions. In addition, the present model, which includes at present no calibration parameters, has been assessed to a large extent with robust periodic unit-cell calculations and for a wide range of parameters (different number and orientation of slip systems, void shapes and orientations, creep exponents and porosity values). This gives confidence that a corresponding three-dimensional model in the same lines as the one proposed here is feasible since the backbone of the present analysis was carried out in a general three-dimensional setting.

Finally, it should be pointed out that several important features present mainly at finite strains, such as lattice rotations, evolution of porosity (e.g., void growth), void shape and orientation are not included in the present analysis (*c.f.* Danas and Ponte Castañeda, 2009b). These additional features would inevitably lead to well known phenomena in porous materials such as material softening, void shape effects, deformation localization (*c.f.* Danas and Ponte Castañeda, 2012) and ultimately void coalescence (see for instance Benzerga, 2002; Pardoen and Hutchinson, 2000; Morin et al., 2015). Such a work is underway and will be presented elsewhere.

Acknowledgments

The work of AM was supported by a CNRS-INSIS PhD fellowship.

Appendix A. Relation between the single crystal and the isotropic matrix behaviors

As seen in subSection 2.3, in the special case of slip systems with identical CRSS and reference slip rate $((\tau_0)^{(s)} = \tau_0,\ (\dot{\gamma}_0)^{(s)} = \dot{\gamma}_0,\ \forall s = 1, K)$, the viscoplastic stress potential of the single crystal is written as

$$U(\boldsymbol{\sigma}) = \frac{\dot{\gamma}_0 \tau_0}{n+1}\left(\frac{\sigma_{eq}}{\tau_0\sqrt{3}}\right)^{n+1}\sum_{s=1}^{K}\left|\sin\left(2\theta^{(s)}+\delta\right)\right|^{n+1}. \tag{A.1}$$

Moreover, when we tend to the limiting case of isotropic matrix, i.e. $K \longrightarrow \infty$, or when we consider "equiangular slip systems" for $K \geqslant 3$,

$$\sum_{s=1}^{K}\left|\sin\left(2\theta^{(s)}+\delta\right)\right|^{n+1} = K.\frac{1}{K}\left|\sin\left(2\theta^{(s)}+\delta\right)\right|^{n+1} \cong K.\frac{2}{\pi}\int_0^{\pi/2}(\sin\theta)^{n+1}d\theta. \tag{A.2}$$

One then recognize a "Wallis" integral (see Wallis, 1656),

$$\int_0^{\pi/2}(\sin\theta)^{n+1}d\theta = \frac{\sqrt{\pi}}{(n+1)}\frac{\Gamma\left(\frac{n+2}{2}\right)}{\Gamma\left(\frac{n+1}{2}\right)}, \tag{A.3}$$

where Γ is the Γ-function. Consequently, expression (2.15) can be readily obtained.

Appendix B. Microstructural tensor in the limiting case of $K \to \infty$ (isotropic matrix)

In the case of slip systems with identical CRSS τ_0 and reference slip-rate $\dot{\gamma}_0$, the compliance tensor $\mathbf{S}_0$ of the linear comparison composite is given by Eq. (3.4) by setting $\lambda^{(s)} = \lambda$ and $\rho^{(s)} = \rho$.

Then using the fact that $\mathbf{F}^{(s)} = \mathbf{K} - \mathbf{E}^{(s)}$ for all $s = 1, K$ leads to

$$\frac{\mathbf{S}_0}{K} = \frac{1}{2\lambda}\left(\frac{1}{K}\sum_{s=1}^{K}\mathbf{E}^{(s)}\right) + \frac{1}{2\rho}\left(\mathbf{K} - \frac{1}{K}\sum_{s=1}^{K}\mathbf{E}^{(s)}\right) + \frac{1}{3\kappa K}\mathbf{J}. \tag{B.1}$$

It is recalled that we need to

Next, in the limit $K \to \infty$, we have the following identity

$$\lim_{K\to\infty}\frac{1}{K}\sum_{s=1}^{K}\mathbf{E}^{(s)} = \frac{1}{2\pi}\int_0^{2\pi}\mathbf{E}(\theta)d\theta = \frac{1}{2}\mathbf{K}, \tag{B.2}$$

where θ denotes any arbitrary slip orientation (see Fig. 1). Using the identity (B.2) into (B.1), one can readily show that in the limit $\rho \to \infty, \kappa \to \infty$ and $K \to \infty$, the microstructural tensor $\mathbf{S}_0^*$ defined in Eq. (3.8) becomes

$$\lim_{K\to\infty}\lim_{\rho\to\infty}\lim_{\kappa\to\infty}\frac{\mathbf{S}_0^*}{K} = \frac{1}{2}\left(\frac{1}{2w}\mathbf{G}\right) \tag{B.3}$$

for general 2D elliptical voids (see Danas, 2008).

References

Abaqus. ABAQUS/Standard Version 6.9, user manual. Simulia Corp., 2009.

Barsoum, I., Faleskog, J., 2007. Rupture mechanisms in combined tension and shear – micromechanics. Int. J. Solids Struct. 44, 5481–5498.

Benzerga, A.A., 2002. Micromechanics of coalescence in ductile fracture. J. Mech. Phys. Solids 50, 1331–1362.

Benzerga, A., Besson, J., 2001. Plastic potentials for anisotropic porous solids. Eur. J. Mech./A 20, 397–434.

Benzerga, A., Besson, J., Pineau, A., 2004. Anisotropic ductile fracture. Part II: Theory. Acta Metall. 52, 4639–4650.

Combaz, E., Bacciarini, C., Charvet, R., Dufour, W., Mortensen, A., 2011. Multiaxial yield behaviour of al replicated foam. J. Mech. Phys. Solids 59, 1777–1793.

Danas, K., 2008. Porous materials with evolving microstructure: constitutive modeling, numerical implementation and applications (Ph.D. thesis). Ecole Polytechnique de Paris.

Danas, K., Aravas, N., 2012. Numerical modeling of elasto-plastic porous materials with void shape effects at finite deformations. Compos.: Part B 43, 2544–2559.

Danas, K., Ponte Castañeda, P., 2009a. A finite-strain model for anisotropic viscoplastic porous media: I – Theory. Eur. J. Mech. A/Solids 28, 387–401.

Danas, K., Ponte Castañeda, P., 2009b. A finite-strain model for anisotropic viscoplastic porous media: II – Applications. Eur. J. Mech. A/Solids 28, 402–416.

Danas, K., Ponte Castañeda, P., 2012. Influence of the Lode parameter and the stress triaxiality on the failure of elasto-plastic porous materials. International Journal of Solids and Structures 49, 1325–1342.

Danas, K., Idiart, M., Ponte Castañeda, P., 2008. A homogenization-based constitutive model for two-dimensional viscoplastic porous media. C.R. Mec. 336, 79–90.

deBotton, G., Ponte Castañeda, P., 1995. Variational estimates for the creep behaviour of polycrystals. Proc. R. Soc. A 448, 121–142.

Eshelby, J.D., 1957. The determination of the elastic field of an ellipsoidal inclusion and related problems. Proc. R. Soc. London A 241, 376–396.

Flandi, L., Leblond, J.-B., 2005. A new model for porous nonlinear viscous solids incorporating void shape effects – I: Numerical validation. Eur. J. Mech. A/Solids 24, 552–571.

Fritzen, F., Forest, S., Bhlke, T., Kondo, D., Kanit, T., 2012. Computational homogenization of elasto-plastic porous metals. Int. J. Plast. 29, 102–119.

Gan, Y., Kysar, J., 2007. Cylindrical void in a rigid-ideally plastic single crystal III: hexagonal close-packed crystal. Int. J. Plast. 23, 592–619.

Gan, Y., Kysar, J., Morse, T., 2006. Cylindrical void in a rigid-ideally plastic single crystal II: experiments and simulations. Int. J. Plast. 22, 39–72.

Gilormini, P., Michel, J.-C., 1998. Finite element solution of the problem of a spherical inhomogeneity in an infinite power-law viscous matrix. Eur. J. Mech. A/Solids 17, 725–740.

Gologanu, M., Leblond, J.B., 1993. Approximate models for ductile metals containing non-spherical voids – case of axisymmetric prolate ellipsoidal cavities. J. Mech. Phys. Solids 41, 1723–1754.

Gurson, A.L., 1977. Continuum theory of ductile rupture by void nucleation and growth. J. Eng. Mater. Technol. 99, 2–15.

Ha, S., Kim, K., 2010. Void growth and coalescence in f.c.c. single crystals. Int. J. Solids Struct. 52, 863–873.

Han, X., Besson, J., Forest, S., Tanguy, B., Bugat, S., 2013. A yield function for single crystals containing voids. Int. J. Solids Struct. 50, 2115–2131.

Hashin, Z., 1962. The elastic moduli of heterogeneous materials. J. Appl. Mech., 143–150

Hashin, Z., Shtrikman, S., 1963. A variational approach to the theory of the elastic behaviour of multiphase materials. J. Mech. Phys. Solids 11, 127–140.

Herve, E., Zaoui, A., 1993. *n*-Layered inclusion-based micromechanical modelling. Int. J. Eng. Sci. 31, 1–10.

Hill, R., 1963. Elastic properties of reinforced solids: Some theoretical principles. J. Mech. Phys. Solids 11, 357–372.

Huang, Y., 1991. A user material subroutine incorporating single crystal plasticity in the abaqus finite element program. Mech Report, Division of Engineering and Aplied Sciences, Harvard University, 178.

Huang, M., Li, Z., Wang, C., 2007. Discrete dislocation dynamics modelling of microvoid growth and its intrinsic mechanism in single crystals. Acta Mater. 55, 1387–1396.

Huang, M., Zhao, L., Tong, J., 2012. Discrete dislocation dynamics modelling of mechanical deformation of nickel-based single crystal superalloys. Int. J. Plast. 28, 141–158.

Hussein, M., Borg, U., Niordson, C., Deshpande, V., 2008. Plasticity size effects in voided crystals. J. Mech. Phys. Solids 56, 114–131.

Idiart, M., Ponte Castañeda, P., 2007. Variational linear comparison bounds for nonlinear composites with anisotropic phases. II: Crystalline materials. Proc. R. Soc. A 463, 925–943.

Kailasam, M., Ponte Castañeda, P., 1998. A general constitutive theory for linear and nonlinear particulate media with microstructure evolution. J. Mech. Phys. Solids 46, 427–465.

Keralavarma, S.M., Hoelscher, S., Benzerga, A.A., 2011. Void growth and coalescence in anisotropic plastic solids. Int. J. Solids Struct. 48, 1696–1710.

Kysar, J.W., 1997. Addendum to 'a user material subroutine incorporating single crystal plasticity in the abaqus finite element program'. Mech Report, Division of Engineering and Aplied Sciences, Harvard University, 178.

Kysar, J., Gan, Y., Mendez-Arzuza, G., 2005. Cylindrical void in a rigid-ideally plastic single crystal. Part I: Anisotropic slip line theory solution for face-centered cubic crystals. Int. J. Plasticity 21, 1481–1520.

Leblond, J., Perrin, G., Suquet, P., 1994. Exact results and approximate models for porous viscoplastic solids. Int. J. Plast. 10, 213–235.

López Jiménez, F., 2014. Modeling of soft composites under three-dimensional loading. Compos.: Part B 59, 173–180.

López Jiménez, F., Pellegrino, S., 2012. Constitutive modeling of fiber composites with a soft hyperelastic matrix. Int. J. Solids Struct. 49, 635–647.

Lopez-Pamies, O., Goudarzi, T., Danas, K., 2013. The nonlinear elastic response of suspensions of rigid inclusions in rubber: II – A simple explicit approximation for finite-concentration suspensions. J. Mech. Phys. Solids 61, 19–37.

Madou, K., Leblond, J., 2012a. A Gurson-type criterion for porous ductile solids containing arbitrary ellipsoidal voids-I: Limit-analysis of some representative cell. J. Mech. Phys. Solids 60, 1020–1036.

Madou, K., Leblond, J., 2012b. A Gurson-type criterion for porous ductile solids containing arbitrary ellipsoidal voids-II: Determination of yield criterion parameters. J. Mech. Phys. Solids 60, 1037–1058.

Mandel, J., 1964. Contribution théorique à létude de lécrouissage et des lois d'écoulement plastique. In: 11th International Congress on Applied Mechanics. Springer, Berlin.

Mbiakop, A., Constantinescu, A., Danas, K., 2015. On void shape effects of periodic elasto-plastic materials subjected to cyclic loading. Eur. J. Mech. Solids 49, 481–499.

Mc Clintock, F., 1968. A criterion for ductile fracture by the growth of holes. J. Appl. Mech. 35, 363–371.

Michel, J.C., Suquet, P., 1992. The constitutive law of nonlinear viscous and porous materials. J. Mech. Phys. Solids 40, 783–812.

Michel, J.-C., Moulinec, H., Suquet, P., 1999. Effective properties of composite material with periodic microstructure: a computational approach. Comput. Methods Appl. Mech. Eng. 172, 109–143.

Miehe, C., Schroder, J., Schotte, J., 1999. Computational homogenization analysis in finite plasticity simulation of texture development in polycrystalline materials. Comput. Methods Applied Mechanics and Engineering 171, 387–418.

Monchiet, V., Charkaluk, E., Kondo, D., 2007. An improvement of Gurson-type models of porous materials by using Eshelby-like trial velocity fields. C.R. Acad. Sci. Paris 335, 32–41.

Monchiet, V., Cazacu, O., Charkaluk, E., Kondo, D., 2008. Macroscopic yield criteria for plastic anisotropic materials containing spheroidal voids. Int. J. Plast. 24, 1158–1189.

Morin, L., Leblond, J.-B., Benzerga, A.A., 2015. Coalescence of voids by internal necking: theoretical estimates and numerical results. J. Mech. Phys. Solids 50, 1331–1362.

Niordson, C.F., Kysar, J.W., 2014. Computational strain gradient crystal plasticity. J. Mech. Phys. Solids 62, 31–47.

Pardoen, T., Hutchinson, J.W., 2000. An extended model for void growth and coalescence. J. Mech. Phys. Solids 48, 2467–2512.

Paux, J., Morin, Brenner, R., Kondo, D., 2015. An approximate yield criterion for porous single crystals. Eur. J. Mech. A/Solids 51, 1–10.

Ponte Castañeda, P., 1991a. The effective mechanical properties of nonlinear isotropic composites. J. Mech. Phys. Solids 35, 45–71.

Ponte Castañeda, P., 1991b. Effective properties in power-law creep. Mech. Creep Brittle Mater. 2, 218–229.

Ponte Castañeda, P., 2002. Second-order homogenization estimates for nonlinear composites incorporating field fluctuations: I-theory. J. Mech. Phys. Solids 50, 737–757.

Ponte Castañeda, P., Willis, J.R., 1995. The effect of spatial distribution on the effective behavior of composite materials and cracked media. J. Mech. Phys. Solids 43, 1919–1951.

Rice, J.R., 1987. Tensile crack tip fields in elastic-ideally plastic crystals. Mech. Mater. 6, 317–335.

Rice, J.R., Tracey, D.M., 1969. On the ductile enlargement of voids in triaxial stress fields. J. Mech. Phys. Solids 17, 201–217.

Rintoul, M.D., Torquato, S., 1997. Reconstruction of the structure of dispersions. J. Colloid Interface Sci. 186, 467–476.

Segurado, J., Llorca, J., 2002. A numerical approximation to the elastic properties of sphere-reinforced composites. J. Mech. Phys. Solids 50, 2107–2121.

Segurado, J., Llorca, J., 2010. Discrete dislocation dynamics analysis of the effect of lattice orientation on void growth in single crystals. Int. J. Plast. 26, 806–819.

Srivastava, A., Needleman, A., 2012. Porosity evolution in a creeping single crystal. Model. Simul. Mater. Sci. Eng. 20.

Srivastava, A., Gopagoni, S., Needleman, A., Seetharaman, V., Staroselsky, A., Banerjee, R., 2012. Effect of specimen thickness on the creep response of a ni-based single-crystal superalloy. Acta Mater. 60, 5697–5711.

Tang, T., Kim, S., Horstemeyer, M., 2010a. Fatigue crack growth in magnesium single crystals under cyclic loading: molecular dynamics simulation. Comput. Mater. Sci. 48, 426–439.

Tang, T., Kim, S., Horstemeyer, M., 2010b. Molecular dynamics simulations of void growth and coalescence in single crystal magnesium. Acta Mater. 58, 4742–4759.

Torquato, S., 2002. Random Heterogeneous Materials: Micorstructures and Macroscopic Properties. Springer.

Traiviratana, S., Bringa, E., Benson, D., Meyers, 2008. Void growth in metals: atomistic calculations. Acta Mater. 56, 3874–3886.

Tvergaard, V., Needleman, A., 1984. Analysis of the cup-cone fracture in a round tensile bar. Acta Metall. 32, 157–169.
Tvergaard, V., Nielsen, K.L., 2010. Relations between a micro-mechanical model and a damage model for ductile failure in shear. J. Mech. Phys. Solids 58, 1243–1252.
Wallis, J., 1656. Arithmetica Infinitorum.
Willis, J.R., 1977. Bounds and self-consistent estimates for the overall properties of anisotropic composites. J. Mech. Phys. Solids 25, 185–202.
Willot, F., Pellegrini, Y., Idiart, M.I., Castañeda, P.P., 2008. Effective-medium theory for infinite-contrast two-dimensionally periodic linear composites with strongly anisotropic matrix behavior: dilute limit and crossover behavior. Phys. Rev. B 78, 104111.
Yerra, S.K., Tekoglu, C., Scheyvaerts, F., Delannay, L., Van Houtte, P., Pardoen, T., 2010. Void growth and coalescence in single crystals. Int. J. Solids Struct. 47, 1016–1029.
Zhao, K., Chen, C., Shen, Y., Lu, T., 2009. Molecular dynamics study on the nano-void growth in face-centered cubic single crystal copper. Comput. Mater. Sci. 46, 749–754.